Applications of optical control materials based on localized surface plasmon resonance effect in smart windows

Ta, Na; Huang, Jing Yi; He, Shuai; Hanggai, W.; Chao, Luo Meng

DOI
10.1007/s42864-024-00273-1

Publication date
2024

Document Version
Final published version

Published in
Tungsten

Tungsten
https://doi.org/10.1007/s42864-024-00273-1

Tungsten
www.springer.com/42864

REVIEW PAPER

Applications of optical control materials based on localized surface plasmon resonance effect in smart windows

Na Ta[1] · Jing-Yi Huang[1] · Shuai He[1] · W. Hanggai[2] · Luo-Meng Chao[1]

Received: 6 October 2023 / Revised: 31 October 2023 / Accepted: 9 November 2023

Abstract
The increasing energy consumption in buildings due to cooling and heating, accounting for over one-third of the total energy consumption in society, has become a growing concern. Therefore, reducing building energy consumption has become an urgent issue for countries worldwide. Windows serve as the primary channel for energy exchange between the indoor and the outdoor environments. While providing natural lighting for occupants, windows are also the weakest link in terms of energy consumption. In recent years, there have been some new and superior coating glass technologies compared to traditional low-emissivity glass. These coatings utilize various optical functional materials to regulate the incident sunlight, aiming to save cooling and heating energy consumption. Materials, such as tungsten-based compounds, vanadium dioxide, lanthanum hexaboride, or copper monosulfide, can absorb near-infrared light to effectively control solar radiation by leveraging the localized surface plasmon resonance (LSPR) effect of nanoparticles. This paper mainly introduces the micro-mechanisms of these materials and provides a detailed summary of the latest advancements in coating materials. The application and effects of these coatings in building energy conservation are emphasized. Finally, the challenges and prospects of LSPR-based smart windows are discussed. It is expected that this review will provide new insights into the application of smart windows in green buildings.

Keywords Tungsten · Localized surface plasmon resonance (LSPR) · Tungsten-based compounds · Vanadium dioxide · Lanthanum hexaboride · Copper monosulfide

1 Introduction

With the acceleration of urbanization and the increasing occurrence of extreme weather events, the energy consumption for cooling and heating in buildings has been continuously rising. This portion of energy consumption now exceeds 40% of the total building energy consumption [1], leading to severe issues such as power shortages in many areas. Therefore, reducing the energy consumption for cooling and heating in buildings has become a focal point in the field of energy conservation. Within building structures, energy exchange between the indoor and the outdoor environments primarily occurs through windows. Modern buildings increasingly strive for spacious visual areas, resulting in larger glass areas in windows [2, 3]. This unavoidably creates a conflict with the energy-saving aspect of building design, leading to significantly increased costs and energy consumption for heating in winter and cooling in summer. Therefore, the key to achieving a comfortable living environment while reducing energy consumption lies in the windows.

The thermal energy of solar radiation is mainly concentrated in the visible (Vis) and near-infrared (NIR) regions (0.3–3 μm), with each region accounting for approximately half of the energy [4]. The solar irradiance under air mass (AM) 1.5 conditions is shown in Fig. 1. For window glass, high Vis (0.38–0.76 μm) is essential to ensure natural daylighting, regardless of the cooling or heating requirements. NIR light (0.76–2.5 μm) should be blocked

✉ W. Hanggai
H.Gai@tudelft.nl

✉ Luo-Meng Chao
2017993@imust.edu.cn

1 College of Science, Inner Mongolia University of Science and Technology, Baotou 014010, China

2 Fundamental Aspects of Materials and Energy, Faculty of Applied Sciences, Delft University of Technology, 2629JB Delft, The Netherlands

Published online: 28 May 2024

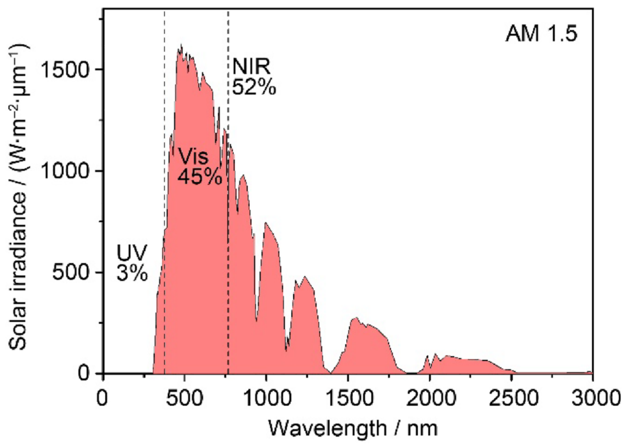

Fig. 1 Solar spectrum irradiance at the situation of AM 1.5

during summer for cooling purposes but be transmitted indoors during winter to introduce solar heat gain. However, currently, there is no perfect solution available to achieve reversible control of NIR for different climatic conditions while maintaining high Vis transmittance.

The most widely promoted product in the field of energy-saving glass is low-emissivity (Low-E) glass [5]. Low-E glass is a film system product composed of multilayered metals such as silver coated on the surface of the glass. Its coating layer has high transparency for Vis light and high reflection for infrared rays, which has excellent heat shielding effects and good light transmittance compared to ordinary glass and traditional architectural coated glass [6]. Low-E glass is usually coated by magnetron sputtering, and it is currently made into a center-controlled sandwich structure, which requires vacuum equipment, uses high airtight composite adhesives, is made up of two or three pieces of glass, and bonded with an aluminum alloy frame containing desiccant. This approach would lead to high costs, making it difficult to popularize in developing countries. In addition to this, Low-E glass also causes light pollution and other multiple issues, including inevitable aging failures [7]. Therefore, in recent years, researchers have been devoted to developing new functional materials and coatings to control the incidence of sunlight and ensure indoor living comfort. From the perspective of Vis light transmittance, these materials can be roughly divided into two categories: a type of material that exhibits color-changing effects under the influence of electric fields, light exposure, or changes in environmental temperature is known as electrochromic, photochromic, or thermochromic material, respectively. Meanwhile, another type of material leverages the localized surface plasmon resonance (LSPR) effect intrinsic to the nanoparticles. This phenomenon allows for the strong absorption of NIR from sunlight, while ensuring high transmittance of Vis light, thus producing a transparent heat shielding effect.

The color-changing materials undergo changes in shape, structure, or phase in response to external stimuli, resulting in color changes and reversible transformations between transparent and opaque states, thereby controlling the incidence of sunlight. Typical examples of electrochromic materials include conductive polymers, such as polyaniline and polypyrrole, inorganic metal oxides, such as WO_3 and TiO_2, and nematic liquid crystals [8–11]. Under the influence of an electric field, these materials undergo changes in their charge state or molecular arrangement, resulting in color variations. However, electrochromic smart windows typically require electricity, electrical equipment, additional operating power, and expensive manufacturing processes, which limit their large-scale application [12]. Similar to electrochromic materials, photochromic materials undergo reversible color changes under illumination at specific wavelengths. These materials include organic substances, such as fulgides, diarylethenes, spiropyrans, spirooxazines, azobenzenes [13], and inorganic substances, such as V_2O_5, WO_3, Nb_2O_5, TiO_2 [14–17]. Organic photochromic materials undergo a coloring process under ultraviolet light, but typically require Vis light to restore their original color. Inorganic photochromic materials usually form electron–hole pairs under illumination, leading to oxidation–reduction reactions or changes in elemental valence states, thereby causing color changes. High coloration contrast, fast reversible switching speed, and high photochemical stability are key measures of the performance of photochromic materials. Thermochromic materials can adjust their colors according to temperature changes. In the application of smart windows, these materials can adjust the transparency of the windows according to temperature changes, thereby automatically adjusting the window's transmittance to sunlight, controlling the energy usage of the house. Such smart windows can adaptively adjust the light according to dynamic environmental temperature. The color change effect is completely driven by the material, so this mechanism is a passive light regulation method. Thermochromic materials that have been studied extensively include VO_2, hydrogels, ionic liquids, liquid crystals, and perovskites [18–23]. Among these materials, hydrogels such as poly(N-isopropylacrylamide) (pNIPAm) have been widely researched recently due to their abrupt response and reasonable activation temperature [12, 24, 25]. Unlike VO_2 and other thermoresponsive hydrogels, pNIPAm has a lower critical solution temperature (LCST) of 32 ℃, which is close to the actual application temperature of thermochromic windows. Above the LCST, the hydrated polymer chains will collapse into globules, making the polymer insoluble in water. Therefore, the window transitions from a transparent state to an opaque state.

The above-mentioned color-changing materials can indeed regulate sunlight to achieve a good thermal control effect indoors, but due to the greatly reduced Vis light transmittance after changing color (some are almost opaque), it seriously affects the field of view. However, another type of inorganic compounds based on LSPR can regulate NIR while maintaining high Vis light transmittance. The LSPR effect is a phenomenon that occurs on the surface of metallic nanoparticles [26]. It arises from the resonance oscillation of free electrons in the metallic nanoparticles when they are excited by photons under specific conditions. The generation of the LSPR effect involves the optical properties and electron structure of the metallic nanoparticles. In these particles, the free electrons in the metal can move freely, forming an electron gas, known as a plasmon [27]. When the nanoparticles are exposed to light, the electric field of the photons excites the free electrons on the surface of the nanoparticle, causing these electrons to resonate oscillate, as shown in Fig. 2. The condition for resonance to occur is that the frequency of the photons matches the inherent plasmonic frequency of the metallic nanoparticles. When these two are equal, the photon energy and the plasmonic oscillations of the metallic nanoparticle resonate, forming LSPR. Under the LSPR effect, the resonant oscillation of the surface electrons in the metallic nanoparticles leads to the amplification and local enhancement of the electric field. This results in notable changes in the absorption, scattering, and transmission spectra. In the absorption spectrum, LSPR will cause enhanced light absorption within a specific wavelength range [28]. In the scattering spectrum, LSPR will cause enhanced light scattering and frequency shift. The LSPR effect is closely related to factors, such as shape, size, and composition of the metallic nanoparticles. By adjusting these parameters, position, intensity, and wavelength range of the LSPR effect can be regulated, thereby achieving precise control over the optical properties of the metallic nanoparticles.

It is worth noting that the LSPR effect is not limited to metallic nanostructures and has also been observed in certain semiconductors with high densities of free charge carriers. In recent years, nanomaterials that have been studied more include tungsten-based compounds, vanadium dioxide, rare-earth hexaborides, copper sulfides, and so on [29–33]. The nanoparticles of these materials often show strong NIR absorption properties induced by LSPR. In finite systems like nanoparticles, the behavior of free electrons is confined, leading to the LSPR effect. This resonance frequency ω_{LSPR} is determined by the size and shape of the nanostructure, as well as the dielectric functions of both the particle and the surrounding medium. Practical applications based on LSPR often harness its strong scattering or absorption properties, tunable optical extinction, or the enhancement of local electric fields [34]. For applications in smart windows, the desired LSPR frequency should fall within the Vis or infrared (IR) spectrum range, ideally with a tunable resonance frequency and minimal energy loss.

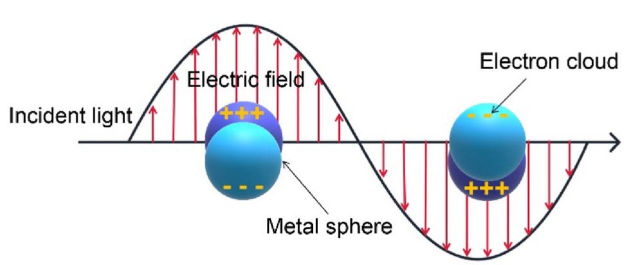

Fig. 2 The schematic diagram of LSPR induced by light

The application of electro-, thermo-, and photochromic materials in the field of smart windows has already been extensively reviewed by numerous researchers [8, 11, 13, 18, 22]. This review paper provides a comprehensive summary of NIR regulating inorganic compounds based on the LSPR effects of nanoparticles, including tungsten-based compounds, vanadium dioxide, lanthanum hexaborides, and copper sulfides. It analyzes and encapsulates the latest developments in terms of their optical properties, NIR shielding mechanisms, optical control characteristics, and more. By comparing different materials, the respective strengths and weaknesses are discussed. Finally, the review offers a perspective on the future developments in the realm of smart windows.

2 Tungsten-based compounds

2.1 Tungsten suboxides

Pure WO_3 is a type of semiconductor material [35], which has high transmittance for Vis light and NIR light [36]. In semiconductor materials, the transition of electrons from the valence band (VB) to the conduction band (CB) results in light absorption, and the absorption edge is determined by the bandgap. The bandgap of pure WO_3 typically falls within the range of 2.6–3.25 eV [35], which places its absorption edge around 400 nm. As a result, most of the Vis light cannot induce intrinsic absorption in tungsten trioxide, ensuring a high Vis light transmittance of the material. Furthermore, the tungsten element only exists in the form of a hexavalent state, which cannot provide additional free electrons. This absence of free electrons does not give rise to a noticeable LSPR effect, thus leading to weak absorption in the NIR region. However, its electrical properties can be regulated by controlling the oxygen content. Oxidized WO_3 is an insulator with a larger bandgap, while reduced WO_{3-x} is a conductive semiconductor. $W_{18}O_{49}$ is a common sub-oxide of tungsten. Research shows that $W_{18}O_{49}$ nanostructures have a high LSPR absorption characteristics [37]. Previous researchers believed that there were some unsaturated oxygen atoms on the surface of $W_{18}O_{49}$ nanoparticles, forming surface oxygen vacancies. These surface defects can cause local charge redistribution and electron oscillations, leading to the emergence of the LSPR effect [38, 39]. However, recent research determined through density functional theory calculations that the lattice pairs of W^{5+}–W^{5+} spaced at 1.3 nm are responsible for the intrinsic LSPR effect of $W_{18}O_{49}$ [40]. The energy level caused by W^{5+} ions localizes high-concentration electrons in a small space, with W^{5+}–W^{5+} pairs serving as localized free electron reservoirs, bringing about an intrinsic LSPR effect. In the electronic structure, the 5d orbital of W is split into a triply degenerate t_{2g} orbital with lower energy and a doubly degenerate e_g orbital with higher energy. The emergence of W^{5+} causes the t_{2g} orbital to move downward, becoming a local energy level in the bandgap. Transitions from this local level to above the Fermi level contribute significantly to the wide-range photoresponse in the Vis–NIR region, as illustrated in Fig. 3. However, localized electrons cannot move freely through the crystal like those in the conduction band, therefore the LSPR absorption range of $W_{18}O_{49}$ is insensitive to shape and size, which is consistent with the experimental results [41].

Currently, there are various methods to prepare $W_{18}O_{49}$, among which the solvothermal method is more frequently adopted [41–43]. By controlling the type and amount of the solvent and the W source, it is possible to achieve $W_{18}O_{49}$ nanomaterials with various morphologies and sizes, such as nanorods, nanofibers, nanobundles, nanograins, nanoassemblies, nanoplates, and nanoparticles as depicted in Fig. 4a–j. The absorption curve of the $W_{18}O_{49}$ solution prepared by Zhong et al. shows lower values in the Vis light range [43], and marked increase in the NIR region (Fig. 4k), which indicates that $W_{18}O_{49}$ possesses NIR shielding properties. However, there isn't a sharp increase in the absorption as it transitions from Vis to NIR; instead, there's a gentle rise between 700 and 1100 nm. This gradual ascent implies a suboptimal shielding effect against the majority of the sunlight's energy concentrated in this range. A film made from a mix of $W_{18}O_{49}$ nanorods and polydimethylsiloxane (PDMS) (as shown in Fig. 4l) mirrored this absorption trend (Fig. 4m). The Vis light transmittance surpassed 60%, gradually diminishing as it approached the NIR spectrum. Thus, for applications like smart windows, there's room for improvement in the optical properties of $W_{18}O_{49}$ at the shorter wavelengths of the NIR spectrum.

2.2 Tungsten bronzes

Tungsten bronze (M_xWO_3) is a non-stoichiometric compound where M represents the insertable cation in the crystal structure of WO_3, and x denotes the concentration

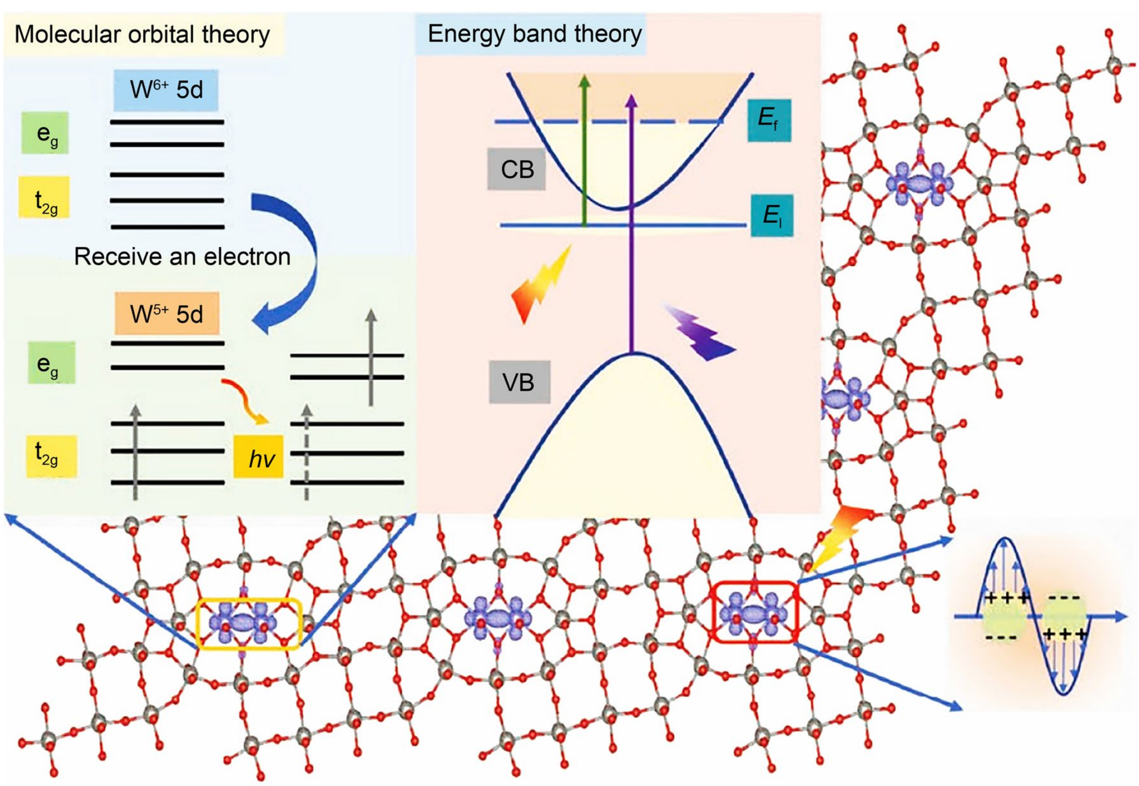

Fig. 3 Schematic diagram of probable electrons transition process under light irradiation for $W_{18}O_{49}$. E_f and E_l stand for Fermi level and localized level, respectively. Reproduced with permission from Ref. [40]. Copyright 2022, Wiley

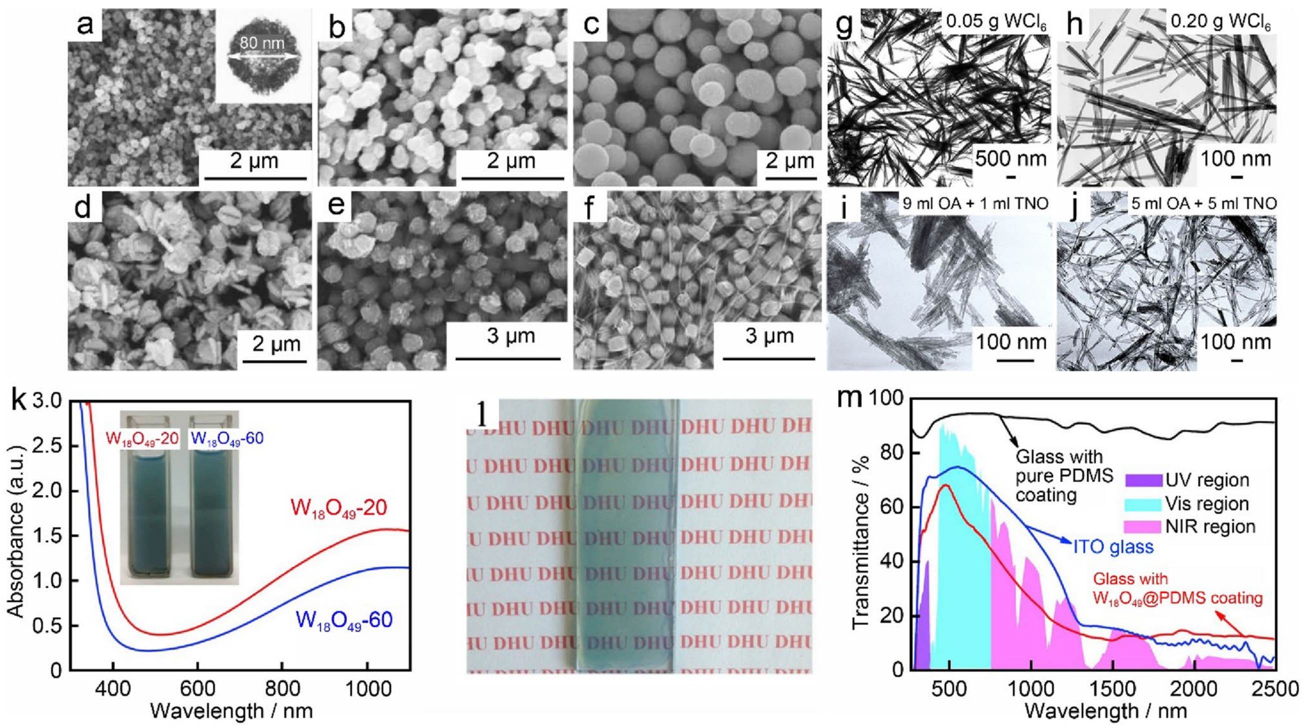

Fig. 4 Scanning electron microscopy (SEM) images of the $W_{18}O_{49}$ nanomaterials synthesized by solvothermal reactions in an ethanol solution containing **a** 7.5 mmol·L^{-1}, **b** 15 mmol·L^{-1}, and **c** 50 mmol·L^{-1} $W(EtO)_6$ at 200 ℃ for 24 h (where Et represents ethyl) [41]; SEM images of $W_{18}O_{49}$ samples synthesized using mixtures of **d** 5 mmol·L^{-1} $W(EtO)_6$ + 10 mmol·L^{-1} WCl_6, **e** 7.5 mmol·L^{-1} $W(EtO)_6$ + 7.5 mmol·L^{-1} WCl_6, and **f** 10 mmol·L^{-1} $W(EtO)_6$ + 5 mmol·L^{-1} WCl_6 as tungsten sources in propanol (T = 200 °C; t = 24 h) [41]; transmission electron microscope (TEM) images of $W_{18}O_{49}$ samples **g, h** synthesized with different amount of WCl_6 in the starting solution and **i**, **j** samples synthesized with different solvent (where OA represents oleic acid and TNO represents tri-n-octylamine) [42]; **k** absorbance of $W_{18}O_{49}$ solution and **l** photos of the flexible $W_{18}O_{49}$@PDMS film and **m** corresponding transmittance (ITO represents indiumtin oxide) [43]. Reproduced from with permission from Refs. [41–43].Copyright 2012, American Chemical Society; Copyright 2016, Elsevier; Copyright 2020, Elsevier, respectively

of the cation. The insertion of cations leads to changes in the electronic structure and optical properties of these materials. M can be alkali metals, alkaline-earth metals, rare-earth elements, or monovalent cations, such as H^+ and NH_4^+ [32]. WO_3 has a simple stoichiometry and possesses a variety of distinct crystal structures, all of which are formed by interconnected WO_6 octahedra that share corners, constituting a three-dimensional network and which can be viewed as variants of the distorted cubic ReO_3 crystal structure [44], tungsten atoms are linked to oxygen atoms by covalent bonds [45, 46]. In M_xWO_3, cations are inserted to the sub-lattice, which not only changes the crystal lattice but also introduces charges, further altering the electronic structure. Tungsten bronze typically exhibits three crystal structures: cubic, tetragonal, and hexagonal structures, as shown in Fig. 5. The crystal structures of tungsten bronze depend on the M and the x, and the maximum value of x depends on the crystal structure and the cation [47–50]. Cubic structures are limited to $x \leq 1.0$, tetragonal to $x \leq 0.6$, and hexagonal to $x \leq 1/3$. But some appear to have lower limits, e.g., tetragonal Na_xWO_3 can only be prepared up to ~ 0.5, but tetragonal K_xWO_3 can go up to 0.6 [34, 51].

The NIR absorption characteristics of tungsten bronzes are mainly attributed to the LSPR effect of its nanoparticles [52–54] and small polaron conversion [55–57]. In tungsten bronze, there is a large number of small polarons. Whenever a cation enters the structure of tungsten bronze, it injects a corresponding number of free electrons into the conduction band. The lattice ions move due to the electrons in the conduction band and are accompanied by polarization, generating an electric field that in turn acts on the electrons, causing lattice distortion. In this way, the electron moves together with the lattice distortion, leading to the small polaron transition between W^{5+} and W^{6+}, as shown in Fig. 6a. Labeling two adjacent W as A and B, the process is represented as follows, where hv and E_{phonon} represents the photon and phonon energy, respectively.

$$hv + W(A)^{5+} + W(B)^{6+} \rightarrow W(A)^{6+} + W(B)^{5+} + E_{phonon} \quad (1)$$

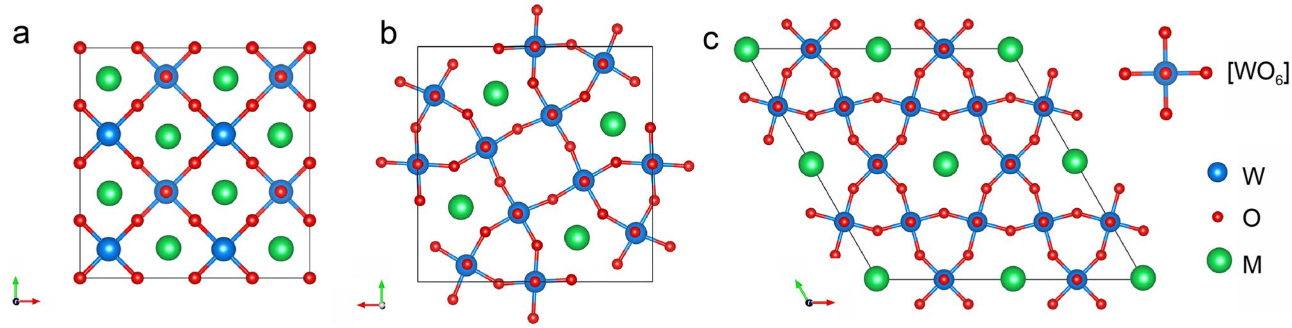

Fig. 5 Crystal structure of tungsten bronze: **a** cubic structure, **b** tetragonal structure, **c** hexagonal structure [32]. Reproduced with permission from Ref. [32]. Copyright 2019, Elsevier

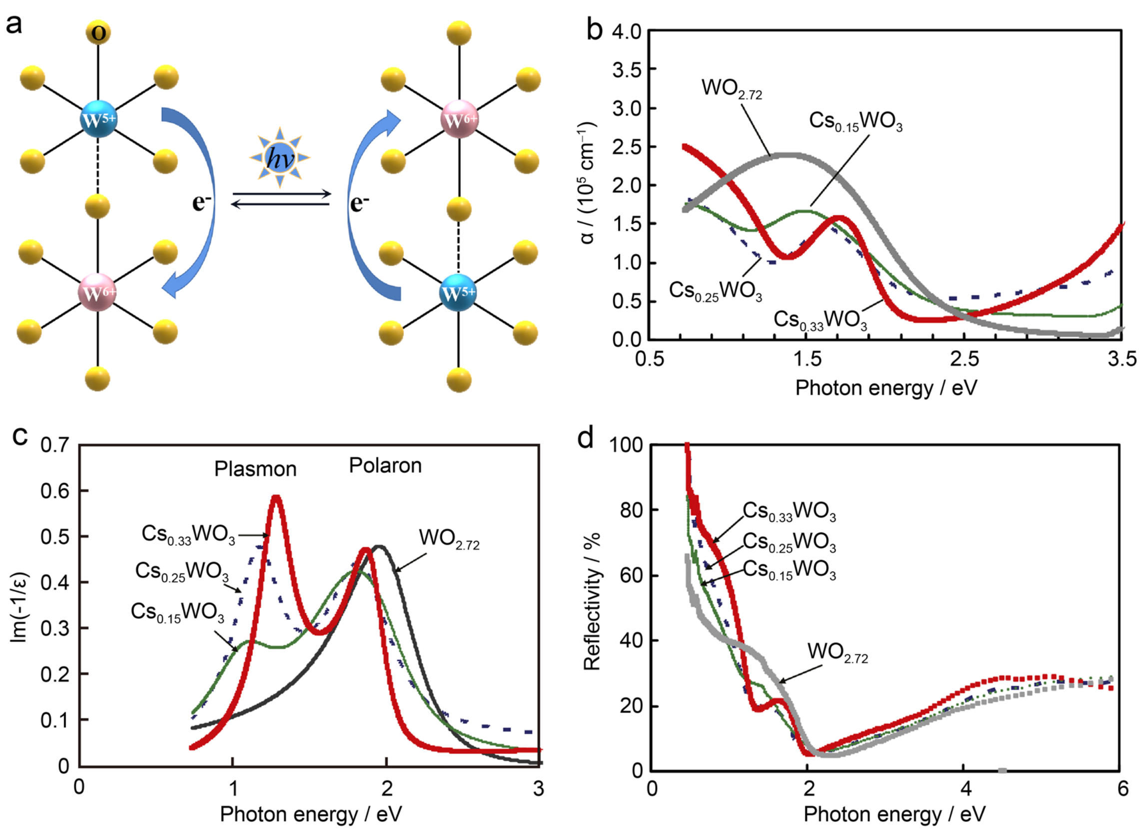

Fig. 6 **a** Schematic diagram of small polaron absorption; **b** absorption coefficients, **c** energy loss functions, and **d** reflectivity of Cs_xWO_3 ($x=0.15$, 0.25, and 0.33) and $WO_{2.72}$ [55]. Reproduced with permission from Ref. [55]. Copyright 2012, Springer Nature

According to Adachi et al.'s analysis of Cs_xWO_3 [55], the asymmetrically shaped peak appearing near 1.5 eV in the absorption spectrum of Fig. 6b matches the features of the small polaron absorption. In the energy loss spectrum of Fig. 6c, besides the feature peak of the small polaron, a bulk plasmon feature peak also emerges. The reflectivity curve in Fig. 6d displays a distinct minimum around 2 eV, followed by a sharp increase at lower energies, a behavior characteristic of free electron plasmas. When Cs is introduced into WO_3, the crystal structure changes from monoclinic to hexagonal, Cs dissociates into Cs^+, and supplies electron to the local energy level and the conduction band. At the maximum value of x at 0.33, the maximum number of electrons occupies the conduction band, and LSPR absorption becomes the major absorption mode for nanoparticles, while polaron absorption provides a minor contribution. Therefore, the primary NIR absorption of

Cs_xWO_3 is not intrinsic absorption but is believed to be absorption generated by the interaction of free electrons in nanoparticles with external electromagnetic waves (i.e., LSPR).

The NIR absorption properties of tungsten bronzes are closely related to the LSPR effect, which in turn depends heavily on the composition, the size, and the morphology of the nanoparticles. Hence, by regulating these factors, the NIR absorption characteristics of tungsten bronze can be optimized. However, precise control over particle size and shape in the synthesis of tungsten bronze nanoparticles remains a significant challenge. Cheref et al. successfully fabricated hexagonal cesium tungsten bronze with various aspect ratios (AR) by adjusting experimental parameters in the thermal decomposition process, as depicted in TEM images shown in Fig. 7a-g (Fig. 7h shows a schematic diagram of hexagonal columns with different AR) [58]. The LSPR effect of the nanoparticles manifests as strong extinction in the NIR region. As can be observed from the extinction curve (Fig. 7i), the extinction peak varies continuously in the NIR region with the change in AR, correlating with the AR-dependent band splitting of the LSPR in both transverse and longitudinal modes. This indicates that combining particle morphology with the anisotropy of the crystal structure, and controlling particle size and AR, can regulate the LSPR response of tungsten bronze nanoparticles across the entire NIR region. From the perspective of smart window applications, the AR-dependent LSPR response evidently affects the shielding performance of the sample against solar radiation (Fig. 7j), providing insights for designing energy-saving materials with varying functionalities. Apart from the AR modulation methods, the research by Tegg et al. has confirmed that the strong LSPR energy of Na_xWO_3 can be continuously adjusted by varying the Na content [59].

From the perspective of NIR shielding, the tungsten bronze series that is currently mainly studied is doped with monovalent cations such as alkali metals (Li, K, Na, Cs, Rb)

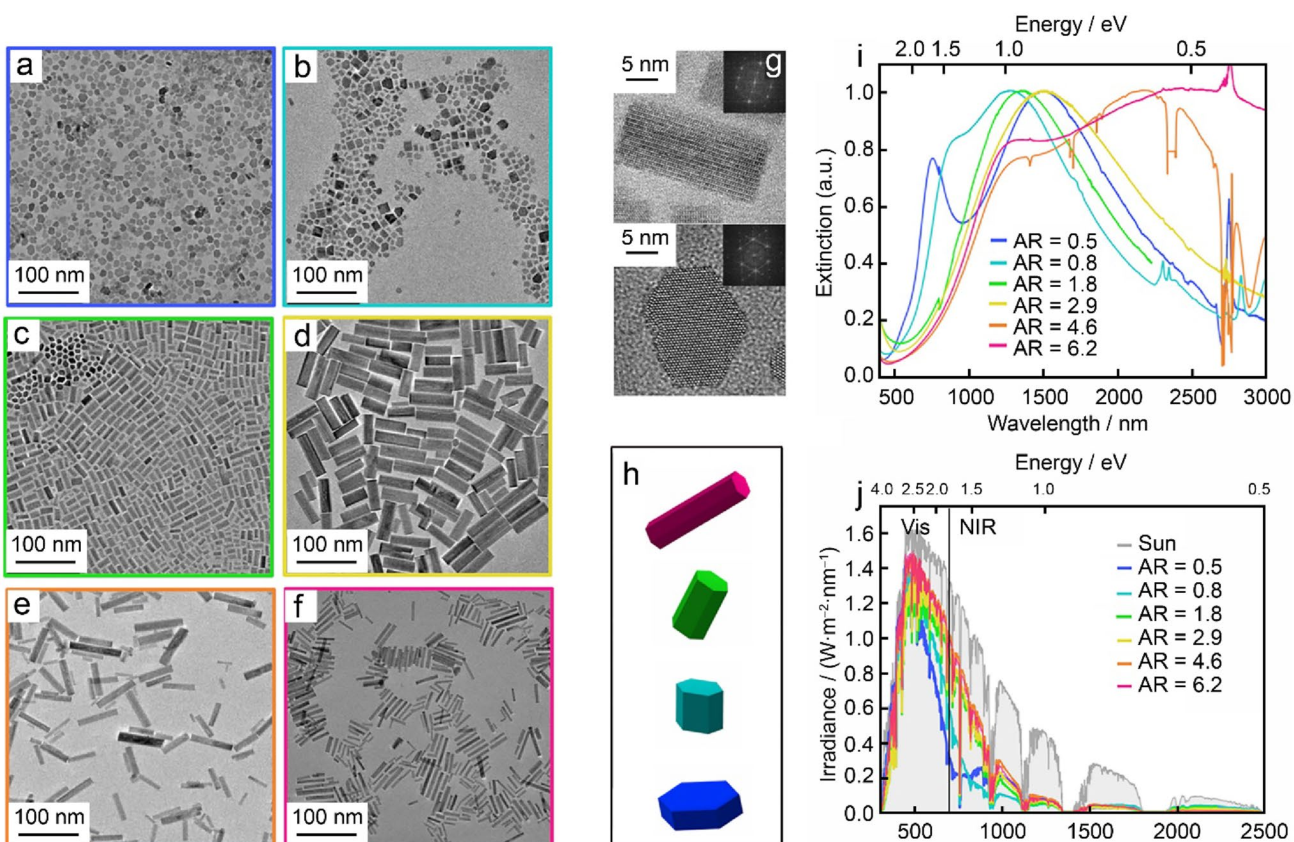

Fig. 7 **a–f** TEM images of the hexagonal cesium tungsten bronze nanocrystals with varied aspect ratios (AR = 0.5, 0.8, 1.8, 2.9, 4.6, 6.2, respectively); **g** high-resolution TEM images showing the lattice structure of the prismatic plane (from **c**) and the basal plane (from **b**); **h** schematic diagram of hexagonal columns with different AR; **i** extinction spectra of the colloidal hexagonal cesium tungsten bronze nanocrystals with varied AR corresponding to the **a–c**; **j** corresponding solar transmission spectra filtered by above samples, where gray line represents solar irradiance at sight level [58]. Reproduced with permission from Ref. [58]. Copyright 2022, American Chemical Society

or ammonium [35, 60–64]. These materials have demonstrated strong NIR absorption capabilities along with high Vis light transmittance. Compared to $W_{18}O_{49}$, tungsten bronze possesses enhanced shielding ability in the shorter wavelength region of the NIR spectrum, hence showcasing great application potential. In recent years, researchers have enhanced the NIR shielding capability of nanocrystalline tungsten bronze by means of doping with dual alkali metal cations [35, 36, 65, 66] or partially substituting the W element with Ti, Mo, Pt, etc. [57, 67, 68]. This adjusts the LSPR effect and small polaron absorption of tungsten bronze. Dual cation co-doping not only promotes the formation of W^{5+} to boost the LSPR effect but also facilitates the bonding between W^{5+} and oxygen. This can enhance the

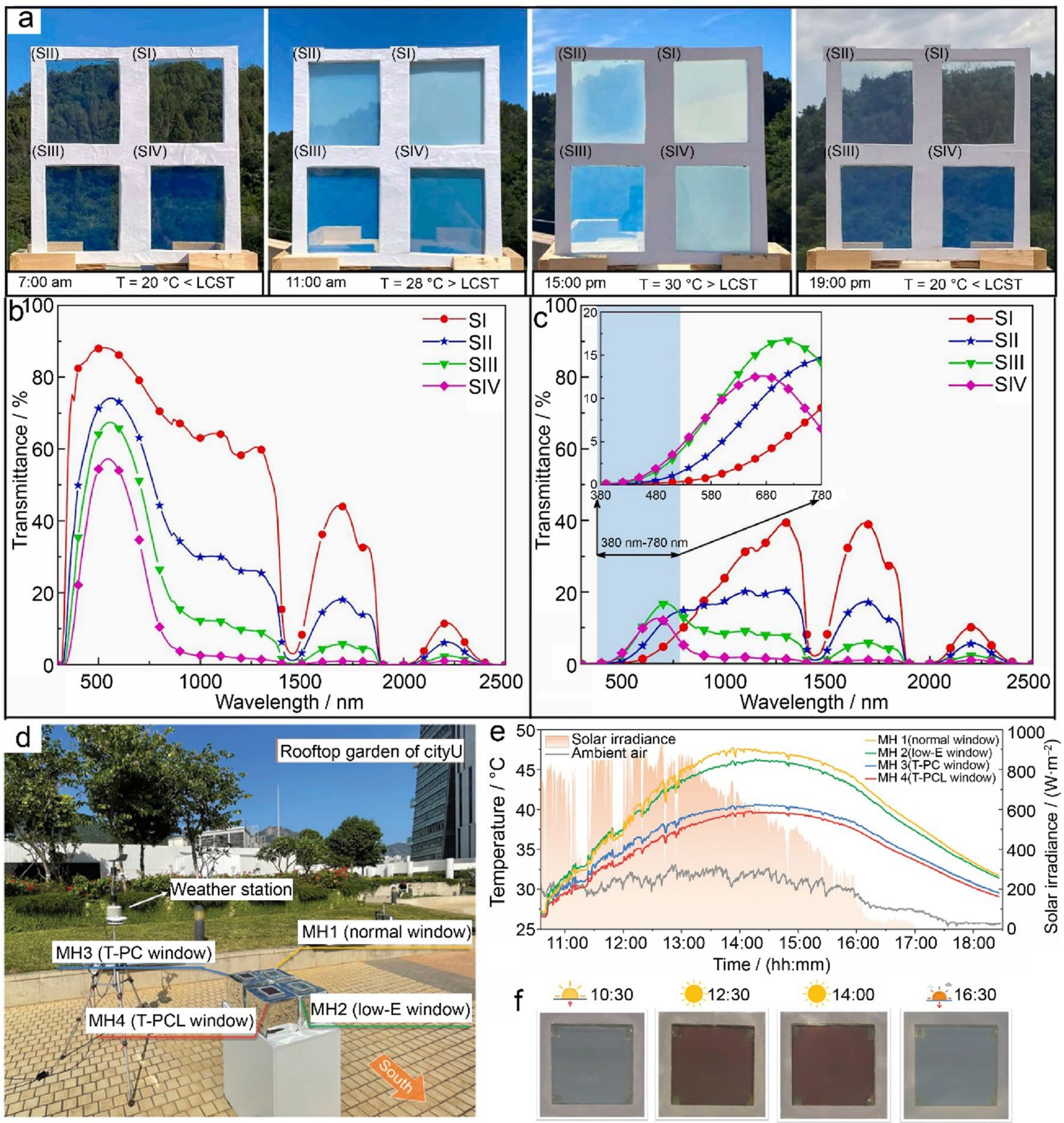

Fig. 8 **a** Actual photo of polyvinyl alcohol-pNIPAm/$Li_mCs_nWO_3$ (LCWO) composite hydrogel smart window at different times of the day, **b, c** transmittance spectra of these windows before **a** and after **b** phase transition (sample SI: LCWO = 0 g·mL^{-1}, SII: LCWO = 8.35×10^{-4} g·mL^{-1}, SIII: LCWO = 1.67×10^{-3} g·mL^{-1}, SIV: LCWO = 3.34×10^{-3} g·mL^{-1}) [69]; **d** model house field test for the normal window, Low-E window, T-PC window and T-PCL window (T-PC window: H-$MAPbI_{3-x}Cl_x$ T-Perovskite and $Cs_{0.33}WO_3$ coated window, T-PCL window: T-Perovskite, $Cs_{0.33}WO_3$ and Low-E layer triple-coated window), **e** indoor temperature curves for these model house field test on the 3rd November, 2021 in Hong Kong, **f** reversible color of the T-PCL window throughout the testing day [70]. Reproduced with permission from Ref. [69, 70]. Copyright 2022, Elsevier; Copyright 2022, John Wiley and Sons, respectively

absorption of small polarons, significantly improving NIR shielding in the 730–1100 nm range. When elements like Mo partially replace the W element, the absorption of small polarons also significantly increases. However, as the doping amount continues to rise, free electrons tend to become localized, suppressing the LSPR effect and diminishing the NIR absorption capability of the particles.

In practical applications, tungsten bronze is often used in conjunction with other materials. For example, by harnessing the self-heating properties when it absorbs NIR light, tungsten bronzes can be combined with thermochromic materials such as pNIPAm or T-Perovskites [69, 70]. The heat generated by tungsten bronze is utilized to facilitate the color-changing process of thermochromic materials, thereby enhancing its optical modulation capabilities, as shown in Fig. 8. In general, tungsten bronze materials can maintain a high Vis light transmittance while also having exceptional NIR shielding capability. They have promising applications in buildings located in hot climate areas, while their energy-saving effects may not be very pronounced in cold regions during winter.

3 Vanadium dioxide

Vanadium dioxide (VO_2) is a typical transition metal oxide that undergoes a reversible metal–insulator phase transition around 68 ℃ [71]. Below this temperature, it acts as an insulator, while above this temperature, it becomes metallic. This phase transition is accompanied by significant changes in its electrical conductivity and optical properties, making VO_2 highly valuable in many applications. Due to its phase transition characteristics, VO_2 can block more NIR radiation as the temperature rises, thereby reducing the heat inside

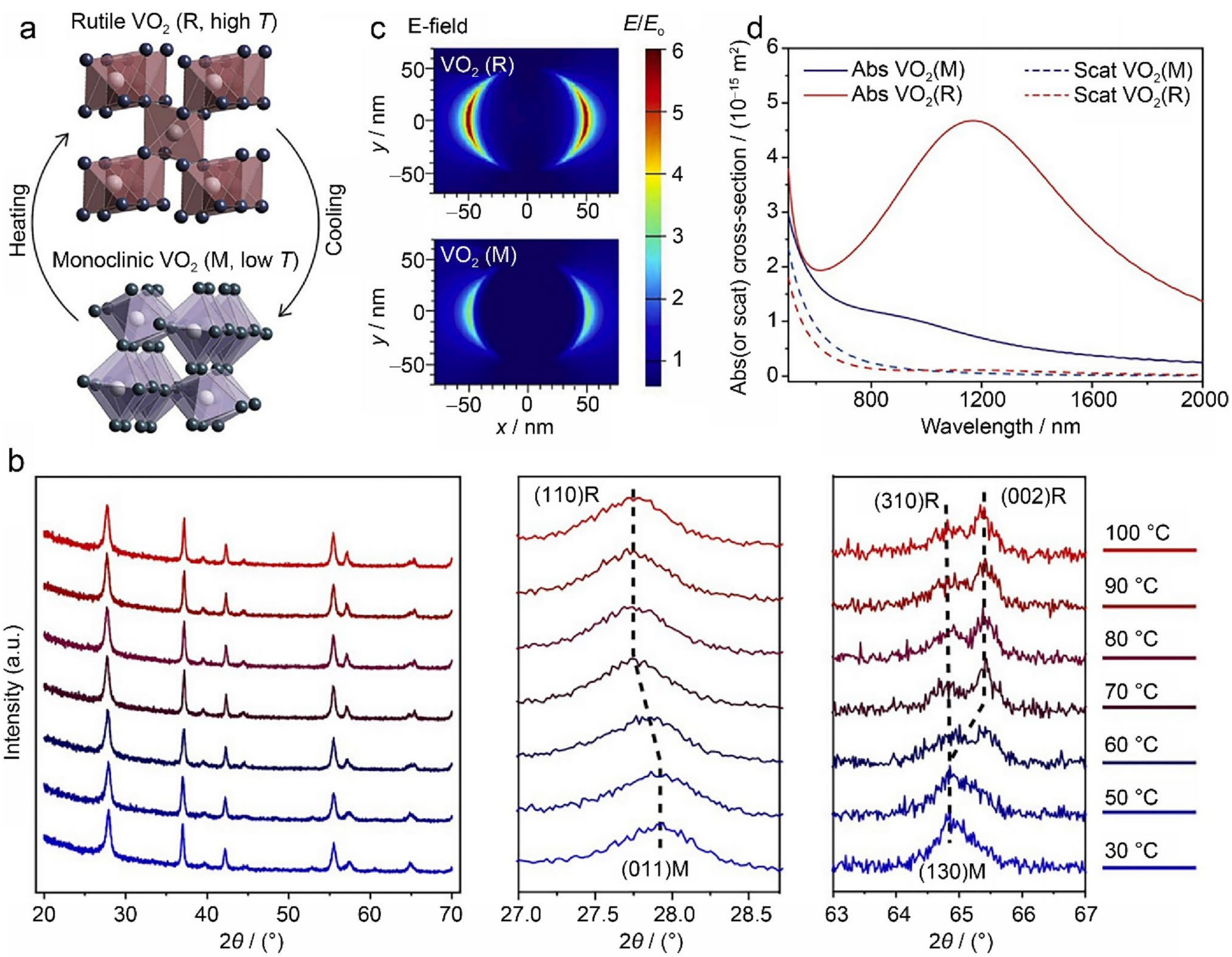

Fig. 9 **a** Crystal phase transition of VO_2 between the high-temperature R phase and the low-temperature M phase; **b** X-ray diffraction analysis of VO_2 at different temperatures; **c** electric field of VO_2 nanoparticles in PDMS matrix at R/M phase; **d** simulated absorbance and scattering of VO_2 nanoparticles in PDMS matrix at R/M phase [73]. Reproduced with permission from Ref. [73]. Copyright 2020, Elsevier

buildings or vehicles. When the temperature is lower, the NIR transmittance significantly increases, which has garnered a lot of attention in the field of smart windows and thermal control coatings [72].

Above the phase transition temperature, the crystal structure of VO_2 is rutile (R phase), while below this temperature, it adopts a monoclinic structure (M phase), as illustrated in Fig. 9a, b [73]. With changes in temperature, there is a reversible transition between these two phases. The LSPR effect of VO_2 becomes pronounced in the R phase and is quenched in the M phase [72–75]. This can be clearly observed from the electric field distribution in Fig. 9c and the simulated absorption and scattering cross section in Fig. 9d.

Various methods have been reported to modulate the LSPR effect of VO_2, enhancing its optical response to better suit applications in the smart windows. These include optimizing the geometric structure of the VO_2 nanoarrays [74, 76], doping metallic nanoparticles into VO_2 thin films to regulate its crystallinity, grain shape, and surface morphology [77, 78], surface treatments of continuous VO_2 films [79, 80], altering the strain-induced local dielectric environment [75], doping with other elements [81], and adjusting the thickness of the coating layer of VO_2 nanoparticles [82], among others.

In Fig. 10a, a hexagonal cylindrical array is designed on a glass substrate [76]. Through finite element method calculations, it was found that by changing parameters, such as radius, height, and spacing of the cylinders, the position of the LSPR absorption peak can be tuned (as shown in Fig. 10b). Compared to single VO_2 nanoparticle, the periodic cylindrical structure of VO_2 exhibits a certain red-shift in the absorption peak. This may be related to a certain degree of overlap in the near-field light field between adjacent particles (Fig. 10c). Based on the transmission results, this kind of nanoparticle array offers better regulatory performance for high-density solar energy with wavelengths around 1000 nm (Fig. 10d). Ke et al. used the nanosphere lithography technique to prepare periodic VO_2 nanoparticle arrays (Fig. 10e) [74]. With the increase in particle size and periodic range, a red-shift in LSPR occurred, consistent with the trend in Fig. 10f. Both these theoretical and experimental findings underscore the tunability of VO_2 LSPR.

The reversible change in VO_2's optical properties with temperature has made it one of the most researched inorganic materials for smart windows. This self-tuning capability of optical properties means that VO_2 has potential applications in various climatic regions. However, VO_2 has a relatively low Vis light transmittance, and its NIR regulation capability is still not outstanding. These drawbacks hinder its further development. Additionally, the appearance of VO_2 films is monotonously brown–yellow (Fig. 11a) [83], which is visually somewhat inferior. To address this, Zhao et al. developed a three-layer VO_2/ photochromism/ fluorescence structure (FPV), which not only enhances the Vis light transmittance and solar regulation efficiency, but also allows this structure to dynamically change to other colors depending on the intensity of ultraviolet light (Fig. 11b–f) [84].

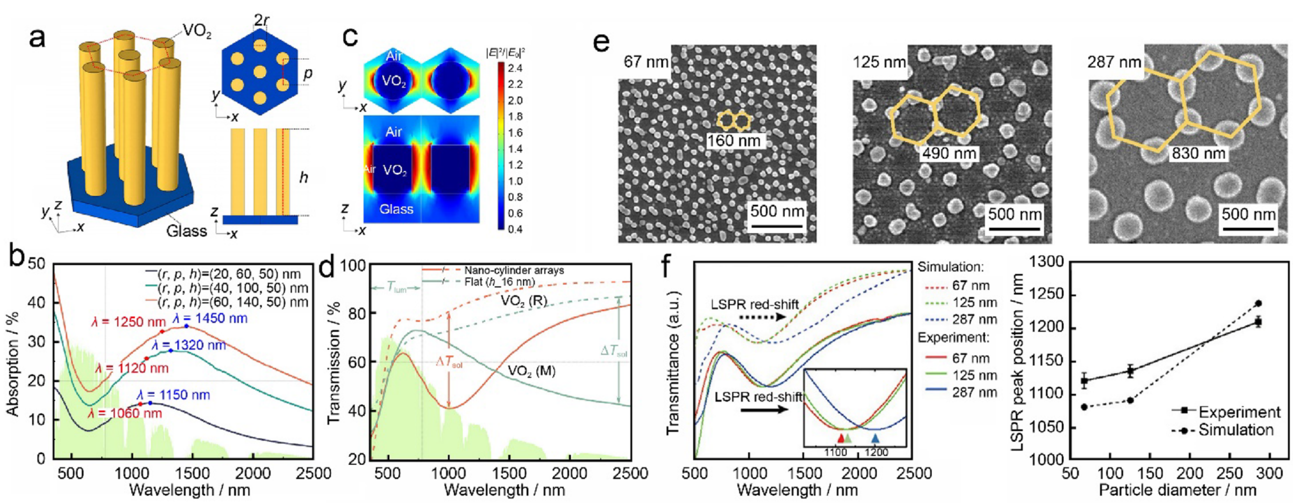

Fig. 10 **a** Schematic of the hexagonal VO_2 nano-cylinder arrays on glass substrate, **b** absorption spectra of VO_2 films (blue and red dots correspond to the absorption peak positions of the periodic structure and a single VO_2 nanoparticle), **c** near-field light intensity profiles of nano-cylinder arrays, **d** transmittance spectra of nano-cylinder arrays and the flat film [76]; **e** SEM images of patterned VO_2 nanoparticle with different sizes, **f** corresponding transmittance spectra of nanoparticle arrays and LSPR position [74]. Reproduced with permission from Refs. [74, 76]. Copyright 2017, American Chemical Society; Copyright 2023, Elsevier

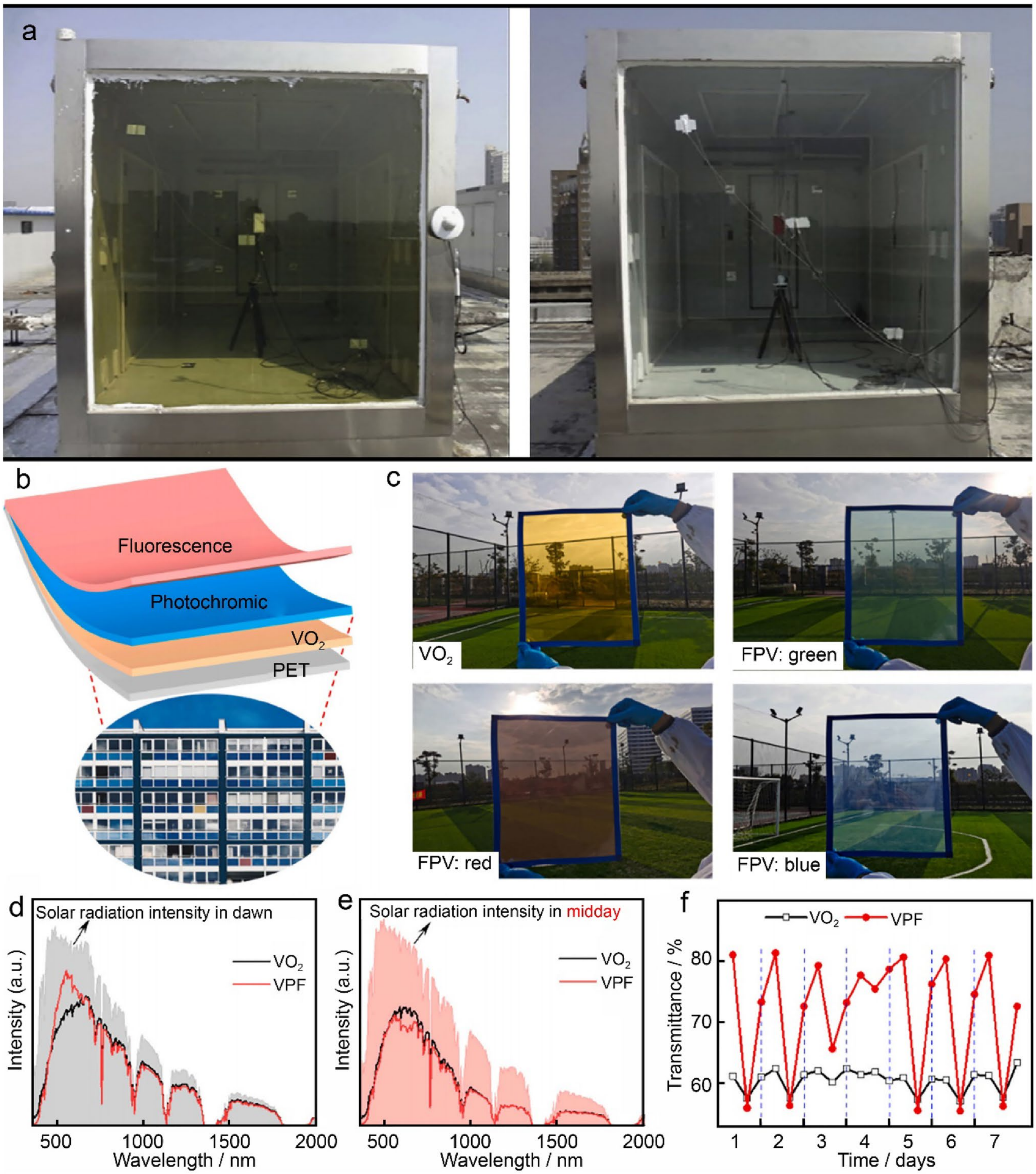

Fig. 11 **a** Photos of a room with VO_2 glazing (left) and a room with ordinary glazing (right) [83]; **b** diagram for illustrating design concept of a flexible three-layer VPF on polyethylene terephthalate substrate; **c** the images of model windows with RGB colors (red: F-red/P-red/VO_2; green: F-green/P-blue/VO_2; blue: F-blue/P-blue/VO_2); **d** house-interior solar intensity of VO_2 film, F-yellow/P-red/VO_2 composite film, and polyethylene terephthalate (PET) film (blank) at dawn; **e** house-interior solar intensity at midday; **f** the transmittance at 550 nm of VO_2 film and F-yellow/P-red/VO_2 composite film at three moments (7:00 AM, 1:00 PM, and 6:00 PM) of a day in one week [84]. Reproduced with permission from Refs. [83, 84]. Copyright 2013, Elsevier; Copyright 2021, Elsevier, respectively

4 Lanthanum hexaboride

Lanthanum hexaboride (LaB_6) is a compound composed of La and B, which is primarily recognized for its exceptional thermionic emission capabilities and is extensively utilized in various domains, such as electron microscopy [85, 86]. LaB_6 adopts a CsCl-type simple cubic structure (space group Pm3m, No. 221), as depicted in Fig. 12a [87]. An octahedron formed by six boron atoms is situated at the center of a cube with lanthanum atoms at its vertices, resulting in LaB_6 having remarkably stable chemical properties. In Fig. 12b, a conduction band crosses over the Fermi level along the *X*–*R* direction of the Brillouin zone. Therefore, LaB_6 manifests metallic properties with a free carrier concentration of approximately 1.45×10^{22} cm^3 [88]. Recent research has revealed that nanoparticles of LaB_6 exhibit a pronounced LSPR effect [89], leading to strong absorption in the NIR light, combined with high transparency in Vis light, promising a bright future in the domain of smart windows. Compared to other plasmonic materials, the electron energy loss spectroscopy peak for LaB_6 nanoparticles lies between 1.1 and 1.4 eV, as shown in Fig. 12c [90]. This range is lower than elemental metals but higher than doped semiconductor materials, positioning LaB_6's unique NIR absorption (or transmission) peak closer to the more energy-dense NIR region of 900–1000 nm, as seen in Fig. 12d.

The LSPR characteristics of LaB_6 can be modulated through various methods, and we have conducted numerous studies both theoretically and experimentally. First-principles calculations reveal that pressure plays a role in adjusting both the intensity and size of the energy loss peak of LaB_6, as illustrated in Fig. 13a. Moreover, the position of the low-energy loss peak is related to the absorption edge in the NIR region [87]. Additionally, doping LaB_6 with other

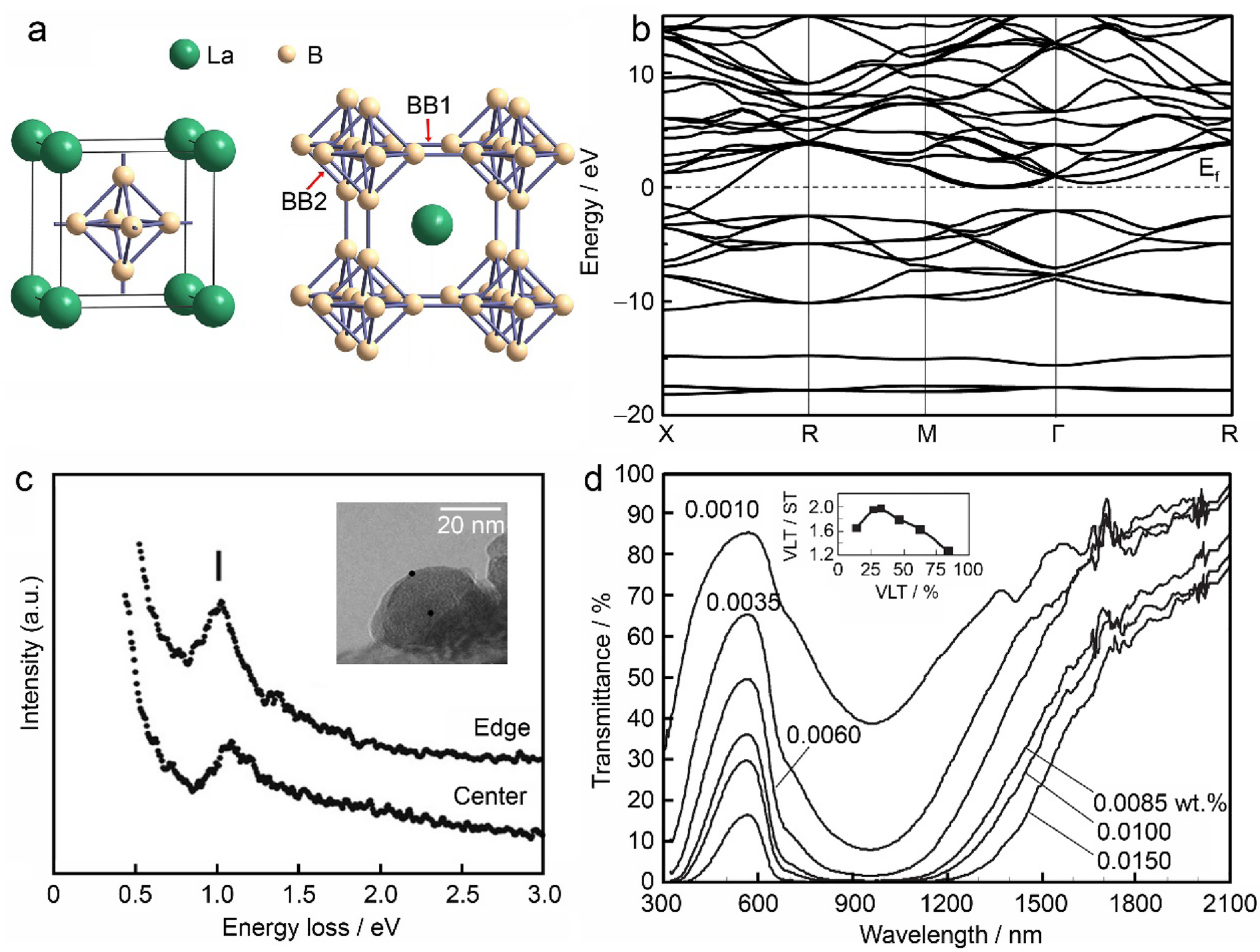

Fig. 12 **a** Crystal structure of LaB_6 [87]; **b** band structure of LaB_6 [87]; **c** electron energy loss spectroscopy of LaB_6 particle shown in the inset [90]; **d** transmittance profiles of LaB_6 dispersions with mean particle size 13 nm diluted to various concentrations, where VLT represents visible light transmittance and ST represents solar transmittance [89]. Reproduced with permission from Refs. [87, 89, 90]. Copyright 2016, Elsevier; Copyright 2010, Springer Nature; Copyright 2011, Elsevier, respectively

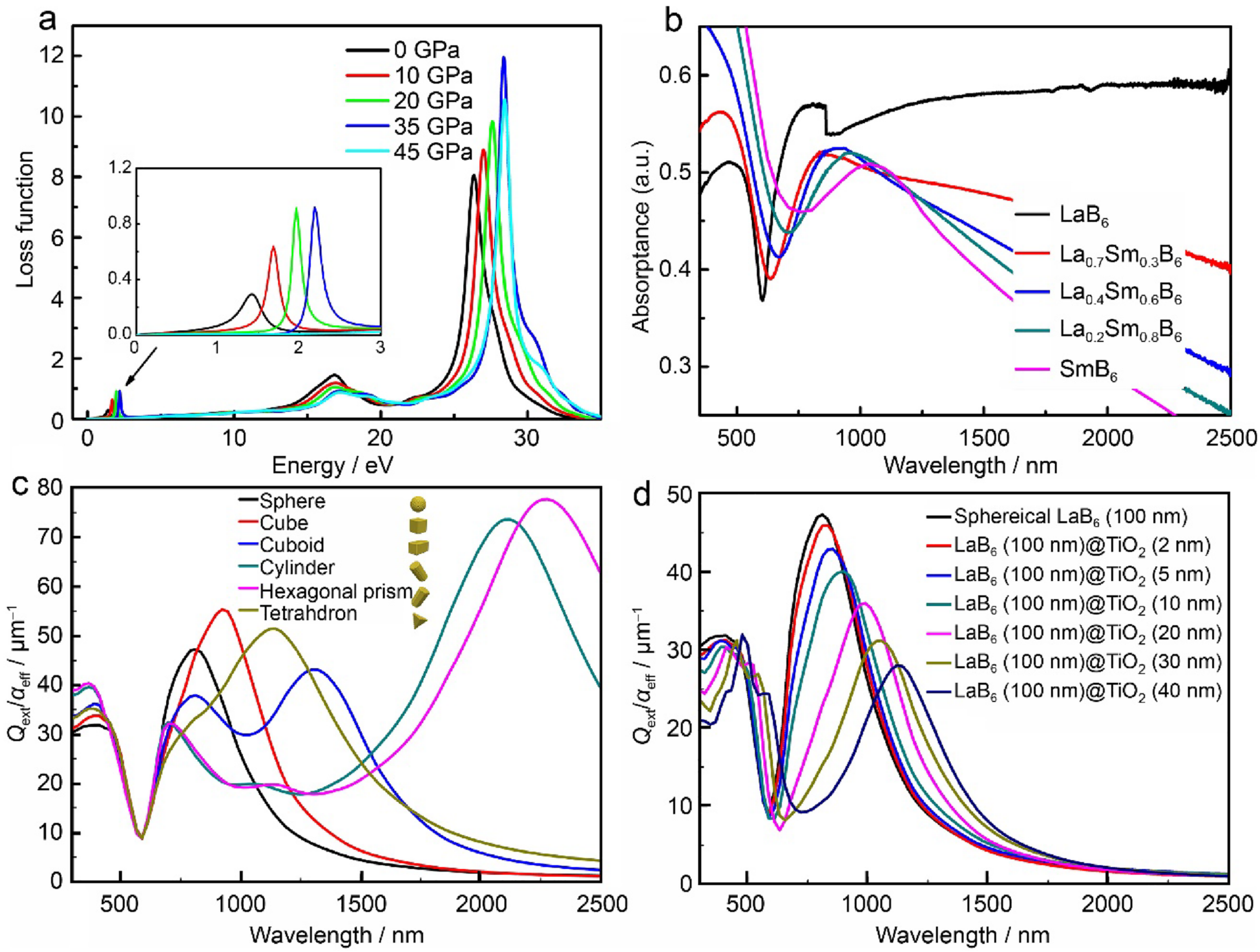

Fig. 13 **a** Energy loss function of LaB_6 at different pressures [87]; **b** optical absorptance of Sm doped LaB_6 [91]; **c** extinction efficiencies of various-shaped LaB_6 particles with an effective radius of 100 nm [93]; **d** extinction efficiencies of LaB_6 spherical particles with different TiO_2 shell thicknesses [93]. Reproduced with permission from Refs. [87, 91, 93]. Copyright 2016, Elsevier; Copyright 2015, Elsevier; Copyright 2021, Elsevier, respectively

rare-earth elements can control its LSPR, subsequently altering the intensity and position of the NIR absorption peak, as shown in Fig. 13b [91, 92]. Our first-principles calculations indicate that when some of the La atoms in LaB_6 are replaced by other rare-earth atoms, the total kinetic energy of electrons near the Fermi surface decreases. This reduction in charge carrier quantity and plasmonic frequency leads to changes in the LSPR characteristics [84]. We also employed the discrete dipole approximation method for theoretical computations on LaB_6 particles with various shapes and coating thicknesses. The results demonstrate that particles with a larger aspect ratio absorb more strongly at longer wavelengths in the NIR, whereas particles with a smaller aspect ratio show stronger absorption at shorter NIR wavelengths, as depicted in Fig. 13c (simulated extinction efficiency Q_{ext}/a_{eff} represents the absorption efficiency of actual samples) [93]. Computations after TiO_2 coating indicate that as the coating thickness increases, both position and intensity of the extinction peak of LaB_6 in the NIR region undergo systematic changes, as shown in Fig. 13d. This is likely associated with the increase in particle size due to thickness variation.

LaB_6 exhibits outstanding shielding capabilities against NIR light, especially at shorter wavelengths within the NIR spectrum. However, its drawback is a narrow and relatively weak transmission peak in the Vis light range, as shown in Fig. 14a [94]. This results in a lower light collection efficiency when used in smart window applications. In Fig. 14b, the LaB_6/PVB composite coating prepared on a glass substrate demonstrates that as the content of LaB_6 increases, transparency significantly decreases and the color darkens [95]. Yet, the insulation rate against NIR radiation is remarkably high. Hence, improving the Vis light transmittance of LaB_6 will be the focus of future research.

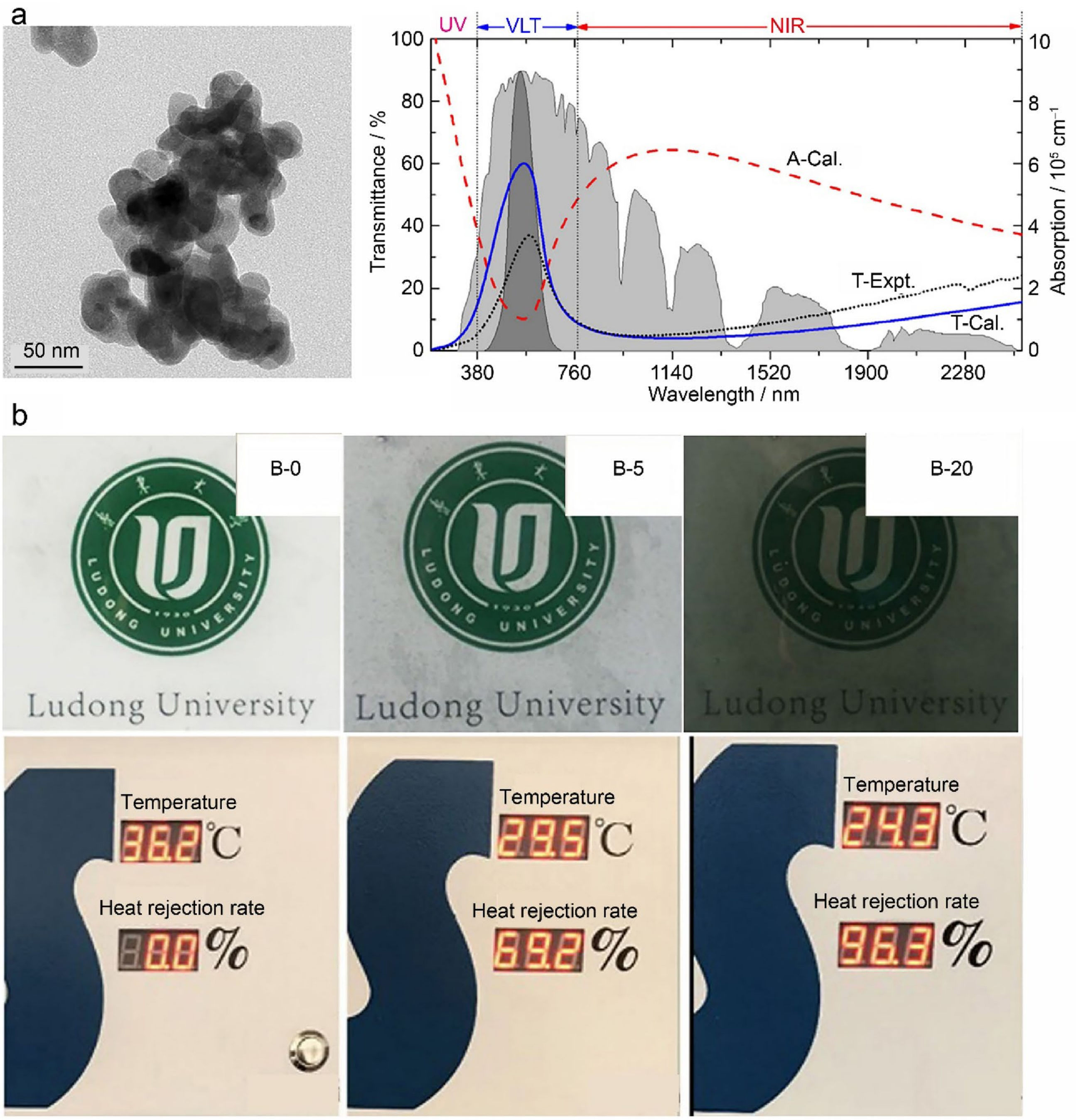

Fig. 14 **a** TEM image of prepared LaB_6 nanoparticles and the transmittance of the corresponding LaB_6/PVB composite resin coatings (dotted line) [94]; **b** photographs of LaB_6/poly(n-butyl acrylate)-r-poly(methacrylate-2-ureido-4[1H]-pyrimidinone) films with different LaB_6 contents and corresponding end temperatures and thermal insulation rates of these films in thermal insulation test [95]. Reproduced with permission from Refs. [94, 95]. Copyright 2016, Elsevier; Copyright 2020, Springer Nature, respectively

5 Copper monosulfide

In recent years, copper-based chalcogenides $Cu_{2-x}E$ (E = S, Se, Te) nanocrystals have garnered significant attention due to their high electrical conductivity, exceptional catalytic performance, substantial specific capacity, and light absorption capabilities [96–100]. These properties make them particularly notable in applications related to sensors, solar cells, and photocatalysis. Among the $Cu_{2-x}E$ nanocrystals, CuS nanocrystals are distinctively recognized for their unique LSPR properties in NIR region [101]. CuS is a p-type semiconductor with a band gap ranging from approximately

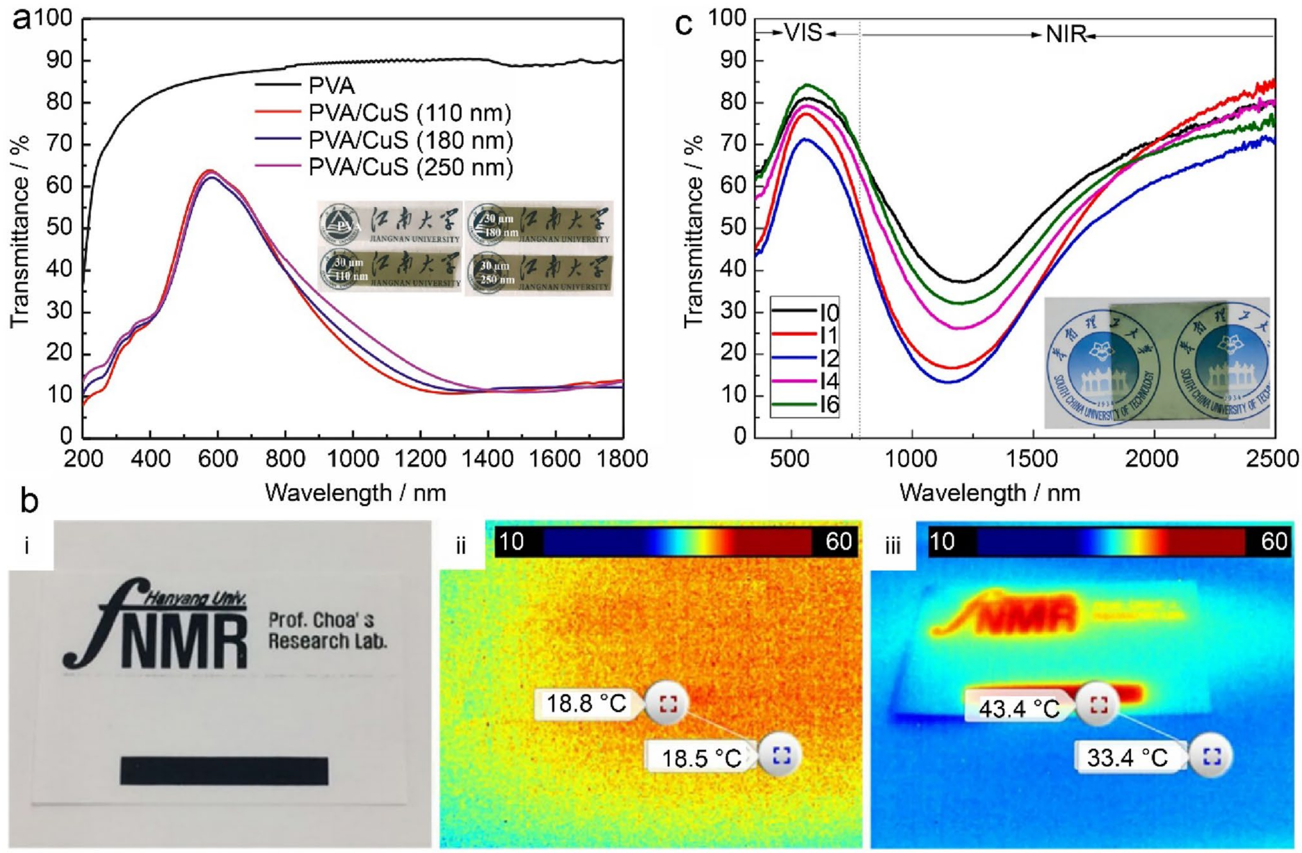

Fig. 15 **a** Transmittance of the polyvinyl alcohol/CuS composite films with 30 μm thickness [33]; **b** a photograph of CuS/PVP nanoparticles printed on white paper and the thermographic images irradiated for different times [103]; **c** transmittance of in doped CuS coatings (I0, I1, I2, I4, and I6 corresponds to the molar ratio of In to Cu was 0, 0.01, 0.02, 0.04 and 0.06, respectively) [104]. Reproduced with permission from Refs. [33, 103, 104]. Copyright 2020, Elsevier; Copyright 2019, Elsevier; Copyright 2021, Elsevier, respectively

2.2 to 2.6 eV. The LSPR absorption peak in the NIR region is predominantly attributed to the inherent copper vacancies in the material. Should these copper vacancies be eliminated, the corresponding LSPR absorption peak would fade away [97]. The Hall effect measurements indicate that for every formula unit in CuS, there exists one-third of a hole [102]. According to the Drude model, this high concentration of p-type free carriers is beneficial for the LSPR in CuS nanostructures. From the transmittance curve of CuS in Fig. 15a [33], it is evident that it exhibits excellent shielding performance in the NIR region, a conclusion that can also be corroborated by the thermographic images in Fig. 15b [103]. The efficiency of NIR shielding can be enhanced through methods such as doping (Fig. 15c) [104]. However, CuS is similar to VO_2 and LaB_6, which does not exhibit the same superior transmittance in the visible region as tungsten bronze does. Additionally, it often displays a brownish hue in thin films.

The LSPR effect of Copper chalcogenides is related to the carrier concentration caused by its copper vacancies. Therefore, besides factors, such as the dielectric constant of the medium, shape, size, and composition, the LSPR resonance wavelength gradually blue shifts to the CuS with the decrease of free carrier concentration [101]. Although CuS exhibits significant LSPR effects in the NIR region, it is characterized by easy photocorrosion and high environmental sensitivity. As a result, coating methods are often required to enhance its optical stability. However, coating can also impact the intensity and position of CuS's LSPR peak [105]. Figure 16a displays CuS nanocrystals with varying SiO_2 shell thicknesses, with their absorption spectra shown in Fig. 16b. As the shell thickness increases, the LSPR peak in the NIR region experiences a red-shift and its intensity gradually decreases. This is likely associated with the reduction in free carrier concentration caused by the SiO_2 coating, a conclusion supported by Hall effect measurements and Mie–Drude model calculations. Moreover, Wei et al. confirmed the revertible shifts of surface-dependent LSPR in CuS nanodisks [101]. Figure 16c illustrates the blue-shift of LSPR with increasing surface treatment cycles at a consistent oxygen exposure time. As depicted in the adjacent schematic, when oleylamine is removed and oxygen

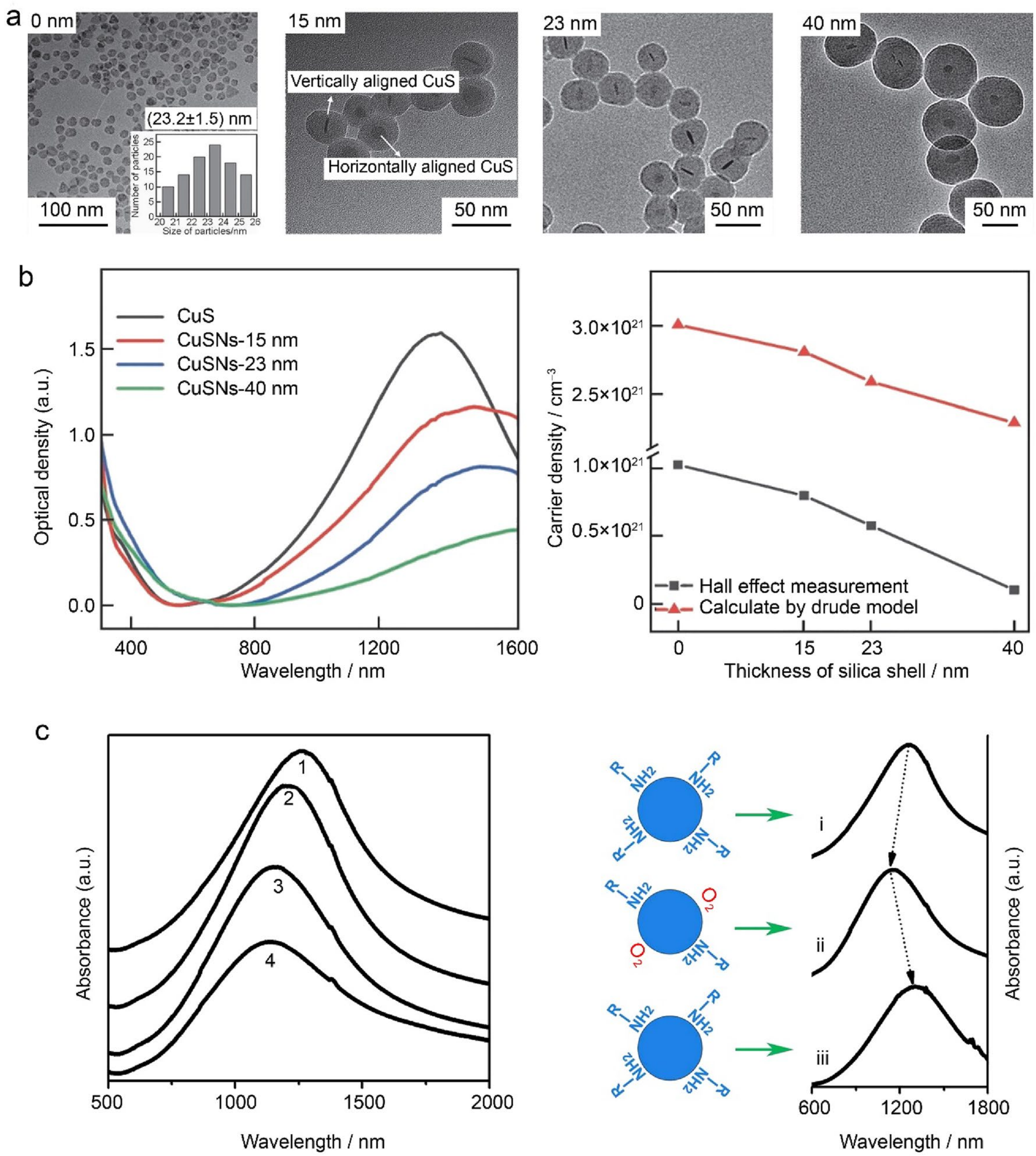

Fig. 16 **a** TEM images of CuS nanocrystals with different SiO_2 shell thicknesses of 0, 15, 23 and 40 nm; **b** corresponding absorption spectra and carrier densities [105]; **c** absorption spectra of CuS nanodisks with increasing surface-treatment cycles (curve 1 to 4 represent an increase in the number of surface-treatment cycles) with identical oxygen exposure time and schematic illustration of the process of LSPRs shifts [101]. Reproduced with permission from Refs. [101, 105]. Copyright 2013, American Chemical Society; Copyright 2023, Springer Nature, respectively

is adsorbed onto the surface of the CuS nanodisks, the LSPR shift toward the blue. However, when the CuS nanodisks are re-passivated with Oleylamine, the LSPR returns to its original position. The surface-dependent shifts of LSPRs are primarily determined by the free hole concentration in CuS nanodisks. This free hole concentration is influenced by the coverage and exchange of surface ligands, as well as the dosage and duration of oxygen exposure.

Compared to LaB_6, the main advantage of CuS is its lower cost and easier preparation of various nanostructural

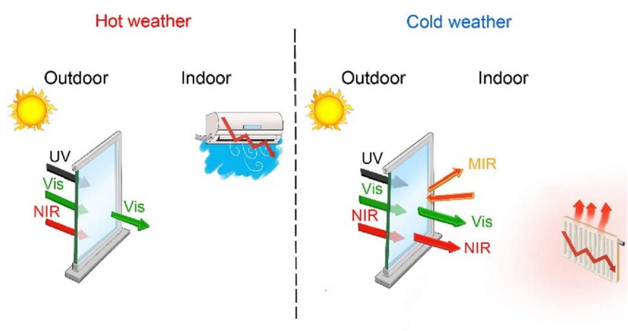

Fig. 17 A working model for an ideal smart window

forms [106]. Therefore, it also has promising development prospects in the field of smart windows.

6 Summary and prospects

An ideal smart window should adapt to various climatic regions. As illustrated in Fig. 17, during hot weather, it should block the UV and NIR rays of the solar spectrum, while allowing Vis light to pass through, thereby reducing cooling energy consumption. Conversely, during cold weather, it should permit NIR to pass through to ensure indoor heat retention. When considering the potential loss of indoor heating energy, the smart window should have a high reflection rate for longer-wavelength mid-infrared rays (with radiation wavelengths of underfloor heating around a few micrometers) to prevent indoor heat from escaping through the window. Materials capable of changing color due to electrical, thermal, or light-induced effects can significantly and reversibly control the incidence of sunlight. However, these materials often substantially reduce the transmittance of Vis light when they change color, resulting in an opaque effect on the corresponding coated glass. This could create an uncomfortable experience for inhabitants when used in buildings. Some metallic compounds with low plasmon frequencies that maintain high Vis light transmittance show promise for applications. These materials absorb UV due to interband transitions and possess LSPR effects that scatter and absorb NIR light. The four plasmonic materials discussed in this article each have their own set of advantages and disadvantages. Tungsten suboxides and tungsten bronzes have excellent NIR shielding capabilities while maintaining a very high transmittance of Vis light. However, their long-term stability in real-world environments is questionable, and their NIR shielding capability is irreversible. Our recent simulations suggest that tungsten bronzes are ideal for energy-saving applications in buildings in hot regions, but it's not as effective in colder regions [107, 108]. The primary advantage of VO_2 is its phase transition property, which shields against NIR in hot weather and automatically increases NIR transmittance in cold conditions. This reversible optical control feature makes it the most researched material in the smart window domain. Yet, VO_2's downsides include its not-so-high transmittance of Vis light and significant room for improvement in its NIR control capacity. LaB_6 exhibits remarkable shielding ability against high-energy solar light around 1000 nm, with notable thermal insulation effects and high chemical stability. However, its disadvantages include a relatively low Vis light transmittance, challenges in synthesizing nano-sized particles, and an irreversible NIR shielding capability. CuS's advantage lies in its cost-effectiveness, making it a relatively affordable option with promising applications. However, its transparent thermal insulation performance is somewhat subpar.

In summary, neither chromogenic nor plasmonic materials offer a perfect solution in the smart window domain currently. Each material has its own set of advantages and drawbacks. The choice should be based on various factors, such as climate, region, budget, and personal preferences. For future research concerning these plasmonic materials, besides continuously optimizing their solar control capabilities, the following points should be considered:

i. The smaller the particle size, the more pronounced the NIR shielding ability. Therefore, in practical applications, particles should be prepared in sizes ranging from a few nanometers to tens of nanometers. While current nanoparticle preparation methods like the solvothermal method can produce smaller-sized particles, but they yield low output, making them unsuitable for large-scale production. On the other hand, solid-state reactions, while facilitating large-scale preparation, often result in micron-sized particles, significantly affecting NIR shielding effects. Therefore, exploring synthesis methods for nanocrystals that are conducive to large-scale production is a promising research direction.
ii. When evaluating the energy-saving effects of these materials on buildings during winter, the reflection rate of these coatings to indoor heat radiation should also be considered, a point often overlooked in current research. For example, the radiation wavelength of underfloor heating is around 8 μm, if these coatings have a high reflection rate in this mid-infrared range, it can prevent indoor heat from escaping through the windows, thus also contributing to energy savings. Therefore, the reflection conditions of these materials' coatings in the mid-infrared should be determined under the same standards and conditions to estimate the energy-saving effects more accurately.

Acknowledgements This research was financially supported by the National Natural Science Foundation of China (No. 52266014), the Natural Science Foundation of Inner Mongolia (No. 2021MS01015), the Program for Young Talents of Science and Technology in Universities of Inner Mongolia Autonomous Region (No. NJYT24062), and the Fundamental Research Funds for Inner Mongolia University of Science & Technology.

Author contributions Na Ta and Jing-Yi Huang wrote the draft; Shuai He revised the manuscript; W. Hanggai and Luo-Meng Chao contributed to conceived the idea of the study. All authors contributed to the writing and revisions.

Data availability The data generated during and/or analyzed in this article are available from the corresponding author on reasonable request.

Declarations

Conflict of interest The authors declare no conflict of interest.

References

1. Evangelisti L, Guattari C, Asdrubali F, Vollaro RDL. An experimental investigation of the thermal performance of a building solar shading device. J Build Eng. 2020;28: 101089. https://doi.org/10.1016/j.jobe.2019.101089.
2. Feng C, Ma F, Wang R, Xu Z, Zhang L, Zhao M. An experimental study on the performance of new glass curtain wall system in different seasons. Build Environ. 2022;219: 109222. https://doi.org/10.1016/j.buildenv.2022.109222.
3. Aiello C, Nicola C, Maddaloni G, Bonati A, Franco A, Occhiuzzi A. Experimental and numerical investigation of cyclic response of a glass curtain wall for seismic performance assessment. Constr Build Mater. 2018;187:596. https://doi.org/10.1016/j.conbuildmat.2018.07.237.
4. Chao L, Li J, Bao L, Ha S, Peng L, Niu J, Liu J, Ma Y. Theoretical and experimental study on optical properties of lanthanum tungsten bronze in visible and near-infrared region. Ceram Int. 2023;49:21017. https://doi.org/10.1016/j.ceramint.2023.03.237.
5. Grosjean A, Baron EL. Longtime solar performance estimations of low-E glass depending on local atmospheric conditions. Sol Energy Mater Sol Cells. 2022;240: 111730. https://doi.org/10.1016/j.solmat.2022.111730.
6. Peng JQ, Curcija DC, Thanachareonkit A, Lee ES, Goudey H, Jonsson J, Selkowitz SE. Comparative study on the overall energy performance between photovoltaic and Low-E insulated glass units. Sol Energy. 2021;214:443. https://doi.org/10.1016/j.solener.2020.12.006.
7. Jelle BP, Kalnæs SE, Gao T. Low-emissivity materials for building applications: a state-of-the-art review and future research perspectives. Energy Build. 2015;96:329. https://doi.org/10.1016/j.enbuild.2015.03.024.
8. Zhao Y, Liu Q, Wang Y, Liu H, Lv M, Cheng P, Fu Y, Li J, He D. Smart windows built with a conductive polymer with net zero energy consumption. Cell Rep Phys Sci. 2022;3(10): 101100. https://doi.org/10.1016/j.xcrp.2022.101100.
9. Yazaki S, Funahashi M, Kato T. An electrochromic nanostructured liquid crystal consisting of π-conjugated and ionic moieties. J Am Chem Soc. 2008;130(40):13206. https://doi.org/10.1021/ja805339q.
10. Liu Y, Cai X, Xiao X, Wang J, Sheng G, Xu G. Preparation of WO_3 gel electrochromic device by simple two-step method. Mater Today Commun. 2022;30: 103090. https://doi.org/10.1016/j.mtcomm.2021.103090.
11. Luo L, Liang Y, Feng Y, Mo D, Zhang Y, Chen J. Recent progress on preparation strategies of liquid crystal smart windows. Crystals. 2022;12(10):1426. https://doi.org/10.3390/cryst12101426.
12. Lei Q, Wang L, Xie H, Yu W. Active-passive dual-control smart window with thermochromic synergistic fluidic glass for building energy efficiency. Build Environ. 2022;222: 109407. https://doi.org/10.1016/j.buildenv.2022.109407.
13. Ke Y, Chen J, Lin G, Wang S, Zhou Y, Yin J, Lee PS, Long Y. Smart windows: electro-, thermo-, mechano-photochromics, and beyond. Adv Energy Mater. 2019;9(39):1902066. https://doi.org/10.1002/aenm.201902066.
14. Gomez-Hermoso-de-Mendoza J, Barud HS, Agnieszka GJ, Tercjak A. Flexible photochromic cellulose triacetate based bionanocomposites modified with sol-gel synthesized V_2O_5 nanoparticles. Carbohydr Polym. 2019;20:50. https://doi.org/10.1016/j.carbpol.2018.12.045.
15. Badour Y, Danto S, Albakour S, Mornet S, Penin N, Hirsch L, Gaudon M. Low-cost WO_3 nanoparticles/PVA smart photochromic glass windows for sustainable building energy savings. Sol Energy Mater Sol Cells. 2023;255: 112291. https://doi.org/10.1016/j.solmat.2023.112291.
16. Li P, Zhang Z, Gao X, Sun H, Peng D, Zou H, Zhang Q, Hao X. Fast self-bleaching Nb_2O_5-based photochromics for high security dynamic anti-counterfeiting and optical storage applications. Chem Eng J. 2022;435(Part1): 134801. https://doi.org/10.1016/j.cej.2022.134801.
17. Miyazaki H, Matsuura T, Ota T. TiO_2 nano-particles based photochromic composite films. Compos Commun. 2018;10:136. https://doi.org/10.1016/j.coco.2018.09.004.
18. Mustafa MN, Abdah MAAM, Numan A, Moreno-Rangel A, Radwan A, Khalid M. Smart window technology and its potential for net-zero buildings: a review. Renew Sustain Energy Rev. 2023;181: 113355. https://doi.org/10.1016/j.rser.2023.113355.
19. Liu S, Tso CY, Du YW, Chao LC, Lee HH, Ho TC, Leung MKH. Bioinspired thermochromic transparent hydrogel wood with advanced optical regulation abilities and mechanical properties for windows. Appl Energy. 2021;297: 117207. https://doi.org/10.1016/j.apenergy.2021.117207.
20. Chen Y, Zhu JT, Ma HB, Chen LL, Li R, Jin P. VO_2/Nickel-bromine-ionic liquid composite film for thermochromic application. Sol Energy Mater Sol Cells. 2019;196:124. https://doi.org/10.1016/j.solmat.2019.03.047.
21. Yu P, Liu J, Zhang WF, Zhao Y, He Z, Ma C, Zhang H, Miao Z, Shen W. Ionic liquid-doped liquid crystal/polymer composite for multifunctional smart windows. Dyes Pigm. 2022;208: 110817. https://doi.org/10.1016/j.dyepig.2022.110817.
22. Wu S, Sun H, Duan M, Mao H, Wu Y, Zhao H, Lin B. Applications of thermochromic and electrochromic smart windows: materials to buildings. Cell Rep Phys Sci. 2023;4(5): 101370. https://doi.org/10.1016/j.xcrp.2023.101370.
23. Zhang Y, Tso CY, Iñigo JS, Liu S, Miyazaki H, Chao CYH, Yu KM. Perovskite thermochromic smart window: advanced optical properties and low transition temperature. Appl Energy. 2019;254: 113690. https://doi.org/10.1016/j.apenergy.2019.113690.
24. Ding Y, Duan Y, Yang F, Xiong Y, Guo S. High-transmittance pNIPAm gel smart windows with lower response temperature and stronger solar regulation. Chem Eng J. 2023;460: 141572. https://doi.org/10.1016/j.cej.2023.141572.
25. Chen G, Wang K, Yang J, Huang J, Chen Z, Zheng J, Wang J, Yang H, Li S, Miao Y, Wang W, Zhu N, Jiang X, Chen Y, Fu J. Printable thermochromic hydrogel-based smart window for

all-weather building temperature regulation in diverse climates. Adv Mater. 2023;35(20):2211716. https://doi.org/10.1002/adma.202211716.
26. Bhatia P, Verma SS. Enhancement of LSPR properties of temperature-dependent gold nanoparticles. Materialstoday Proc. 2023;78(Part4):871. https://doi.org/10.1016/j.matpr.2022.12.020.
27. Fahimi-Kashani N, Orouji A, Ghamsari M, Sahoo SK, Hormozi-Nezhad MR. Chapter: 1 Plasmonic noble metal (Ag and Au) nanoparticles: From basics to colorimetric sensing applications. In: Sahoo S, Hormozi-Nezhad MR, editors. Gold and silver nanoparticles, vol. 1. Amsterdam: Elsevier; 2023.
28. Qin C, Kim JB, Gonome H, Lee BJ. Chapter 19: Plasmonic nanofluids for solar thermal applications. In: Mengüç MP, Light FM, editors. Plasmonics and particles, vol. 421. Amsterdam: Elsevier; 2023.
29. Coşkun M, Altınöz S, Coşkun ÖD. Optical properties of VO_2 spherical nanoparticles. Photon Nanostruct-Fundam Appl. 2022;49:100993. https://doi.org/10.1016/j.photonics.2022.100993.
30. Lin JH, Yan YT, Qi JL, Zha CY. Atomic tailoring-induced deficiency in tungsten oxides for high-performance energy-related devices. Tungsten. 2023;6:269. https://doi.org/10.1007/s42864-023-00232-2.
31. Khan A, Nilam B, Rukhsar C, Sayali G, Mandlekar B, Kadam A. A review article based on composite graphene @tungsten oxide thin films for various applications. Tungsten. 2023;5:391. https://doi.org/10.1007/s42864-022-00158-1.
32. Chao L, Bao L, Wei W, Tegus O. A review of recent advances in synthesis, characterization and NIR shielding property of nanocrystalline rare-earth hexaborides and tungsten bronzes. Sol Energy. 2019;190:10. https://doi.org/10.1016/j.solener.2019.07.087.
33. Yuan H, Li T, Wang Y, Ma P, Du M, Liu T, Yan Y, Bai H, Chen M, Dong W. Photoprotective and multifunctional polymer film with excellent near-infrared and UV shielding properties. Compos Commun. 2020;22: 100443. https://doi.org/10.1016/j.coco.2020.100443.
34. Tegg L, Keast VJ. A Review of alkali tungsten bronze nanoparticles for applications in plasmonics. Plasmonics. 2023;18:49. https://doi.org/10.1007/s11468-022-01749-x.
35. Yang C, Chen JF, Zeng X, Cheng D, Cao D. Design of the alkali-metal-doped WO_3 as a near-infrared shielding material for smart window. Ind Eng Chem Res. 2014;53(46):17981. https://doi.org/10.1021/ie503284x.
36. Yang C, Chen JF, Zeng X, Cheng D, Huan H, Cao D. Enhanced near-infrared shielding ability of (Li, K)-codoped WO_3 for smart windows: DFT prediction validated by experiment. Nanotechnology. 2016;27:075203. https://doi.org/10.1088/0957-4484/27/7/075203.
37. Yan NF, Cui HM, Shi JS, You SY, Liu S. Recent progress of $W_{18}O_{49}$ nanowires for energy conversion and storage. Tungsten. 2023;5:371. https://doi.org/10.1007/s42864-023-00202-8.
38. Yan J, Wang T, Wu G, Dai W, Guan N, Li L, Gong J. Tungsten oxide single crystal nanosheets for enhanced multichannel solar light harvesting. Adv Mater. 2015;27(9):1580. https://doi.org/10.1002/adma.201404792.
39. Lu C, Li J, Chen G, Li B, Lou Z. Self-Z-scheme plasmonic tungsten oxide nanowires for boosting ethanol dehydrogenation under UV-visible light irradiation. Nanoscale. 2019;11(27):12774. https://doi.org/10.1039/C9NR03741A.
40. Lu Y, Jia X, Ma Z, Li Y, Yue S, Liu X, Zhang J. W^{5+}-W^{5+} Pair Induced LSPR of $W_{18}O_{49}$ to sensitize $ZnIn_2S_4$ for full-spectrum solar-light-driven photocatalytic hydrogen evolution. Adv Func Mater. 2022;32(35):2203638. https://doi.org/10.1002/adfm.202203638.
41. Guo C, Yin S, Yan M, Kobayashi M, Kakihana M, Sato T. Morphology-controlled synthesis of $W_{18}O_{49}$ nanostructures and their near-infrared absorption properties. Inorgnic Chemistry. 2012;51(8):4763. https://doi.org/10.1021/ic300049j.
42. Li G, Wu G, Guo C, Wang B. Fabrication of one-dimensional $W_{18}O_{49}$ nanomaterial for the near infrared shielding. Mater Lett. 2016;169:227. https://doi.org/10.1016/j.matlet.2016.01.094.
43. Zhong Q, Macharia DK, Zhong W, Liu Z, Chen Z. Synthesis of hydrophobic $W_{18}O_{49}$ nanorods for constructing UV/NIR-shielding and self-cleaning film. Ceram Int. 2020;46(8):11898. https://doi.org/10.1016/j.ceramint.2020.01.226.
44. Howard CJ, Luca V, Knight KS. High-temperature phase transitions in tungsten trioxide-the last word? J Phys: Condens Matter. 2002;14:377. https://doi.org/10.1088/0953-8984/14/3/308.
45. Kielwein M, Saiki K, Roth G, Fink J, Paasch G, Egdell RG. High-energy electron-energy-loss study of sodium-tungsten bronzes. Phys Rev B. 1995;51:10320. https://doi.org/10.1103/PhysRevB.51.10320.
46. Anders H, Granqvist CG, Wills JM. Electronic structure and optical properties of WO_3, $LiWO_3$, $NaWO_3$, and HWO_3. Phys Rev B. 1996;54:2436. https://doi.org/10.1103/PhysRevB.54.2436.
47. Wiseman PJ, Dickens PG. Neutron diffraction studies of cubic tungsten bronzes. J Solid State Chem. 1976;17(1–2):91. https://doi.org/10.1016/0022-4596(76)90206-1.
48. Ribnick AS, Post B, Banks E. Phase transitions in sodium tungsten bronzes. Nonstoichiometric Compounds. Washington: American Chemical Society. 1963. 246.
49. Owen JF, Teegarden KJ. Optical properties of the sodium-tungsten bronzes and tungsten trioxide. Phys Rev B. 1978;18:3827. https://doi.org/10.1103/PhysRevB.18.3827.
50. Hussin A, Gruehn R, Ritscher CH. Crystal growth of alkali metal tungsten bronzes M_xWO_3 (M = K, Rb, Cs), and their optical properties. J Alloy Compd. 1997;246(1–2):51. https://doi.org/10.1016/S0925-8388(96)02470-X.
51. Shanks HR. Growth of tungsten bronze crystals by fused salt electrolysis. J Cryst Growth. 1972;13–14:433. https://doi.org/10.1016/0022-0248(72)90199-6.
52. Mamak M, Choi SY, Stadler U, Dolbec R, Boulos M, Petrov S. Thermal plasma synthesis of tungsten bronze nanoparticles for near infra-red absorption applications. J Mater Chem. 2010;20(44):152. https://doi.org/10.1039/C0JM02169E.
53. Guo W, Guo C, Zheng N, Sun T, Liu S. Cs_xWO_3 Nanorods coated with polyelectrolyte multilayers as a multifunctional nanomaterial for bimodal imaging-guided photothermal/photodynamic cancer treatment. Adv Mater. 2017;29(4):2144. https://doi.org/10.1002/adma.201604157.
54. Mattox TM, Bergerud A, Agrawal A, Milliron DJ. Influence of shape on the surface plasmon resonance of tungsten bronze nanocrystals. Chem Mater. 2014;26(5):1779. https://doi.org/10.1021/cm4030638.
55. Adachi K, Asahi T. Activation of plasmons and polarons in solar control cesium tungsten bronze and reduced tungsten oxide nanoparticles. J Mater Res. 2012;27:965. https://doi.org/10.1557/jmr.2012.25.
56. Li G, Guo C, Yan M, Liu S. Cs_xWO_3 nanorods: realization of full-spectrum responsive photocatalytic activities from UV, visible to near-infrared region. Appl Catal B-Environ. 2016;183:142. https://doi.org/10.1016/j.apcatb.2015.10.039.
57. Liu JX, Ran S, Fan CY, Qiao YT, Shi F, Yang JY, Chen B, Liu SH. One pot synthesis of Pt-doped Cs_xWO_3 with improved near infrared shielding for energy-saving film applications. Sol Energy. 2019;178:17. https://doi.org/10.1016/j.solener.2018.12.007.
58. Cheref Y, Lochon F, Daugas L. Cleret de Langavant C, Larquet E, Baron A, Gacoin T, Kim J, Dual-band LSPR of tungsten bronze nanocrystals tunable over NIR and SWIR ranges. Chem Mater. 2022;34(21):9795. https://doi.org/10.1021/acs.chemmater.2c02879.

59. Tegg L, Cuskelly D, Keast VJ. Plasmon responses in the sodium tungsten bronzes. Plasmonics. 2017;13:437. https://doi.org/10.1007/s11468-017-0528-y.
60. Lee SY, Kim JY, Lee JY, Song HJ, Lee S, Choi KH, Shin G. Facile fabrication of high-efficiency near-infrared absorption film with tungsten bronze nanoparticle dense layer. Nanoscale Res Lett. 2014;9:294. https://doi.org/10.1186/1556-276X-9-294.
61. Chao L, Sun C, Dou J, Li J, Liu J, Ma Y, Xiao L. Tunable transparency and NIR-shielding properties of nanocrystalline sodium tungsten bronzes. Nanomaterials. 2021;11(3):731. https://doi.org/10.3390/nano11030731.
62. Peng L, Xu Z, Chao L, Zheng D, Yang H, Sun C, Cui H. New energy-saving building developed by using polyethylene glycol/halloysite nanotube energy-storage blanket and heat-insulating glass with $Na_xWO_3@SiO_2$ nano-coating. Sol Energy Mater Sol Cells. 2023;250:112074. https://doi.org/10.1016/j.solmat.2022.112074.
63. Yan M, Gu H, Liu Z, Guo C, Liu S. Effective near-infrared absorbent: ammonium tungsten bronze nanocubes. RSC Adv. 2015;5(2):967. https://doi.org/10.1039/C4RA12471E.
64. Wu X, Wang J, Zhang G, Katsumata K, Yanagisawa K, Sato T, Yin S. Series of M_xWO_3/ZnO (M = K, Rb, NH_4) nanocomposites: combination of energy saving and environmental decontamination functions. Appl Catal B. 2017;201:128. https://doi.org/10.1016/j.apcatb.2016.08.030.
65. Song X, Liu J, Shi F, Fan C, Ran S, Zhang H, Zou Z. Facile fabrication of $KmCsnWO_3$ with greatly improved near-infrared shielding efficiency based on W^{5+}-induced small polaron and local surface plasmon resonance (LSPR) modulation. Sol Energy Mater Sol Cells. 2020;218: 110769. https://doi.org/10.1016/j.solmat.2020.110769.
66. Moon K, Cho JJ, Lee YB, Yoo PJ, Bark CW, Park J. Near infrared shielding properties of quaternary tungsten bronze nanoparticle $Na_{0.11}Cs_{0.22}WO_3$. Bull Korean Chem Soc. 2013;34(3):731. https://doi.org/10.5012/bkcs.2013.34.3.731.
67. Li Q, Deng S, Li D, Yang J, Jin H, Li J. Tungsten bronze Cs_xWO_3 nanopowders doped by Ti to enhance transparent thermal insulation ability for energy saving. J Alloy Compd. 2023;944: 169164. https://doi.org/10.1016/j.jallcom.2023.169164.
68. Wang Q, Li C, Xu W, Zhao X, Zhu J, Jiang H, Kang L, Zhao Z. Effects of Mo-doping on microstructure and near-infrared shielding performance of hydrothermally prepared tungsten bronzes. Appl Surf Sci. 2017;399:41. https://doi.org/10.1016/j.apsusc.2016.12.022.
69. Zhang H, Liu J, Fei S, Li T, Zhang H, Yang D, Li Y, Tian Z, Zhou N. A novel bidirectional fast self-responsive PVA-PNIPAM/$Li_mCs_nWO_3$ composite hydrogel for smart window applications. Chem Eng J. 2022;431(3):133353. https://doi.org/10.1016/j.cej.2021.133353.
70. Liu S, Li Y, Wang Y, Yu KM, Huang B, Tso CY. Near-infrared-activated thermochromic perovskite smart windows. Adv Sci. 2022;9(14):2106090. https://doi.org/10.1002/advs.202106090.
71. Abe H, Terauchi M, Tanaka M, Shin S, Ueda Y. Electron energy-loss spectroscopy study of the metal-insulator transition in VO_2. Jpn J Appl Phys. 1997;36:165. https://doi.org/10.1143/JJAP.36.165.
72. Cui Y, Ke Y, Liu C, Chen Z, Wang N, Zhang L, Zhou Y, Wang S, Gao Y, Long Y. Thermochromic VO_2 for energy-efficient smart windows. Joule. 2018;2(9):1707. https://doi.org/10.1016/j.joule.2018.06.018.
73. Ke Y, Zhang Q, Wang T, Wang S, Li N, Lin G, Liu X, Dai Z, Yan J, Yin J, Magdassi S, Zhao D, Long Y. Cephalopod-inspired versatile design based on plasmonic VO_2 nanoparticle for energy-efficient mechano-thermochromic windows. Nano Energy. 2020;73: 104785. https://doi.org/10.1016/j.nanoen.2020.104785.
74. Ke Y, Wen X, Zhao D, Che R, Xiong Q, Long Y. Controllable fabrication of two-dimensional patterned VO_2 nanoparticle, nanodome, and nanonet arrays with tunable temperature-dependent localized surface plasmon resonance. ACS Nano. 2017;11(7):7542. https://doi.org/10.1021/acsnano.7b02232.
75. Ke Y, Yin Y, Zhang Q, Tan Y, Hu P, Wang S, Tang Y, Zhou Y, Wen X, Wu S, White TJ, Yin J, Peng J, Xiong Q, Zhao D, Long Y. Adaptive thermochromic windows from active plasmonic elastomers. Joule. 2018;3(3):858. https://doi.org/10.1016/j.joule.2018.12.024.
76. Song H, Li H, Ma X, Yin G. Thermochromic performance enhancement by geometric structure optimization of VO_2 nanoarrays for smart window application. Optics Commun. 2023;546: 129763. https://doi.org/10.1016/j.optcom.2023.129763.
77. Li M, Zhang S, Bian L, Sun B, Han J, Zong H, Yan L, Qiao W, Hu Q. Regulating surface morphology and thermochromic properties of VO_2 films by Cu-Ag bimetallic nanoparticles. Surfac Interfac. 2023;37: 102688. https://doi.org/10.1016/j.surfin.2023.102688.
78. Zong H, Zhang S, Bian L, Chen H, Liu Z, Sun B, Qiao W, Yan L, Hu Q, Li M. Preparation and characterization of VO_2/Cu-Zr NPs/VO_2 composite films with enhanced thermochromic properties. J Alloy Compd. 2023;967: 171654. https://doi.org/10.1016/j.jallcom.2023.171654.
79. Li B, Tian S, Qian J, Wu S, Liu B, Zhao X. In situ synthesis of highly dispersed VO_2(M) nanoparticles on glass surface for energy-efficient smart windows. Ceram Int. 2023;49(2):2310. https://doi.org/10.1016/j.ceramint.2022.09.199.
80. Long S, Cao X, Wang Y, Chang T, Li N, Jin L, Ma L, Xu F, Sun G, Jin P. Karst landform-like VO_2 single layer solution: controllable morphology and excellent optical performance for smart glazing applications. Sol Energy Mater Sol Cells. 2020;209: 110449. https://doi.org/10.1016/j.solmat.2020.110449.
81. Wang N, Duchamp M, Xue C, Dunin-Borkowski RE, Liu G, Long Y. Single-crystalline W-doped VO_2 nanobeams with highly reversible electrical and plasmonic responses near room temperature. Adv Mater Interfac. 2016;3(15):1600164. https://doi.org/10.1002/admi.201600164.
82. Zhou Y, Huang A, Li Y, Ji S, Gao Y, Jin P. Surface plasmon resonance induced excellent solar control for $VO_2@SiO_2$ nanorods-based thermochromic foils. Nanoscale. 2013;5(19):9208. https://doi.org/10.1039/C3NR02221H.
83. Ye H, Long L, Zhang H, Bin Xu, Gao Y, Kang L, Chen Z. The demonstration and simulation of the application performance of the vanadium dioxide single glazing. Solar Energy Mater Solar Cells. 2013;117:168. https://doi.org/10.1016/j.solmat.2013.05.061.
84. Zhao S, Shao Z, Huang A, Bao S, Luo H, Ji S, Jin P, Cao X. Dynamic full-color tunability of high-performance smart windows utilizing absorption-emission effect. Nano Energy. 2021;89(Part A):106297. https://doi.org/10.1016/j.nanoen.2021.106297.
85. Chao L, Bao L, Wei W, Tegus O. Optical properties of Yb-doped LaB_6 from first-principles calculation. Mod Phys Lett B. 2016;30(7):1650091. https://doi.org/10.1142/S0217984916500913.
86. Craciun V, Craciun D. Pulsed laser deposition of crystalline LaB_6 thin films. Appl Surf Sci. 2005;247(1–4):384. https://doi.org/10.1016/j.apsusc.2005.01.071.
87. Chao L, Bao L, Wei W, Tegus O, Zhang Z. First-principles study on the electronic structure, phonons and optical properties of LaB_6 under high-pressure. J Alloy Compd. 2016;672:419. https://doi.org/10.1016/j.jallcom.2016.02.179.
88. Kauer E. Optical and electrical properties of LaB_6. Phys Lett. 1963;7(3):171. https://doi.org/10.1016/0031-9163(63)90369-X.
89. Adachia K, Miratsu M. Absorption and scattering of near-infrared light by dispersed lanthanum hexaboride nanoparticles for

solar control filters. J Mater Res. 2010;25:510. https://doi.org/10.1557/JMR.2010.0075.

90. Sato Y, Terauchi M, Mukai M, Kaneyama T, Adachi K. High energy-resolution electron energy-loss spectroscopy study of the dielectric properties of bulk and nanoparticle LaB_6 in the near-infrared region. Ultramicroscopy. 2011;111(8):1381. https://doi.org/10.1016/j.ultramic.2011.05.003.
91. Chao L, Bao L, Shi J, Wei W, Tegus O, Zhang Z. The effect of Sm-doping on optical properties of LaB_6 nanoparticles. J Alloy Compd. 2015;622:618. https://doi.org/10.1016/j.jallcom.2014.10.141.
92. Bao L, Chao L, Wei W, Tegus O. Tunable transmission light in nanocrystalline $La_{1-x}Eu_xB_6$. Mater Lett. 2015;139:187. https://doi.org/10.1016/j.matlet.2014.10.060.
93. Chao L, Sun C, Shu Q, Liu J, Xiao L. Evaluation of the optical properties of various-shaped and core-shell-structured lanthanum hexaboride nanoparticles based on discrete dipole approximation. J Quant Spectrosc Radiat Transfer. 2021;272:107806. https://doi.org/10.1016/j.jqsrt.2021.107806.
94. Xiao L, Su Y, Qiu W, Liu Y, Ran J, Wu J, Lu F, Shao F, Tang D, Peng P. Solar radiation shielding properties of transparent LaB_6 filters through experimental and first-principles calculation methods. Ceram Int. 2016;42(12):14278. https://doi.org/10.1016/j.ceramint.2016.05.105.
95. Liu Q, Zhang C, Yang L, Bai L, Ying L, Wang W, Yang H, Wei D, Chen H. Tailoring LaB_6 nanoparticle-based self-healing film for heat-shielding window. Bull Mater Sci. 2020;43:62. https://doi.org/10.1007/s12034-019-2028-5.
96. Zhao Y, Pan H, Lou Y, Qiu X, Zhu J, Burda C. Plasmonic $Cu_{2-x}S$ nanocrystals: optical and structural properties of copper-deficient copper(I) sulfides. J Am Chem Soc. 2009;131(12):4253. https://doi.org/10.1021/ja805655b.
97. Luther JM, Jain PK, Ewers T, Alivisatos AP. Localized surface plasmon resonances arising from free carriers in doped quantum dots. Nat Mater. 2011;10:361. https://doi.org/10.1038/nmat3004.
98. Hsu SW, Bryks W, Tao AR. Effects of carrier density and shape on the localized surface plasmon resonances of $Cu_{2-x}S$ nanodisks. Chem Mater. 2012;24(19):3765. https://doi.org/10.1021/cm302363x.
99. Liu X, Wang X, Zhou B, Law WC, Cartwright AN, Swihart MT. Size-controlled synthesis of $Cu_{2-x}E$ (E=S, Se) nanocrystals with strong tunable near-infrared localized surface plasmon resonance and high conductivity in thin films. Adv Func Mater. 2013;23(10):1256. https://doi.org/10.1002/adfm.201202061.
100. Lie SQ, Wang DM, Gao MX, Huang CZ. Controllable copper deficiency in $Cu_{2-x}Se$ nanocrystals with tunable localized surface plasmon resonance and enhanced chemiluminescence. Nanoscale. 2014;6(17):10289. https://doi.org/10.1039/C4NR02294G.
101. Wei T, Liu Y, Dong W, Zhang Y, Huang C, Sun Y, Chen X, Dai N. Surface-dependent localized surface plasmon resonances in CuS nanodisks. ACS Appl Mater Interfaces. 2013;5(21):10473. https://doi.org/10.1021/am4039568.
102. Nozaki H, Shibata K, Ohhashi N. Metallic hole conduction in CuS. J Solid State Chem. 1991;91(2):306. https://doi.org/10.1016/0022-4596(91)90085-V.
103. Kwon YT, Lim GD, Kim S, Ryu SH, Lim HR, Choa YH. Effect of localized surface plasmon resonance on dispersion stability of copper sulfide nanoparticles. Appl Surf Sci. 2019;477:204. https://doi.org/10.1016/j.apsusc.2017.11.006.
104. Gao Q, Wu X, Huang T. Novel energy efficient window coatings based on In doped CuS nanocrystals with enhanced NIR shielding performance. Sol Energy. 2021;220:1. https://doi.org/10.1016/j.solener.2021.02.045.
105. Meng C, Huang M, Li Y. Optimized preparation of CuS@SiO_2 core-shell nanoparticles with strong LSPR absorption and excellent photostability for highly efficient solar-driven interfacial water evaporation. Chem Res Chin Univ. 2023;39:697. https://doi.org/10.1007/s40242-023-3124-z.
106. Rokade AA, Jin YE, Park SS. Facile synthesis of plate-like CuS nanoparticles and their optical and photo-thermal properties. Mater Chem Phys. 2018;207:465. https://doi.org/10.1016/j.matchemphys.2017.12.077.
107. Peng L, Chao L, Xu Z, Yang H, Zheng D, Wei B, Sun C, Cui H. High-efficiency energy-saving buildings utilizing potassium tungsten bronze heat-insulating glass and polyethylene glycol/expanded energy storage blanket. Energy. 2022;255: 124585. https://doi.org/10.1016/j.energy.2022.124585.
108. Chao L, Sun C, Peng L, Li J, Sun M, Bao L, Liu J, Ma Y. Passive energy-saving buildings realized by the combination of transparent heat-shielding glass and energy storage cement. Constr Build Mater. 2023;365: 130023. https://doi.org/10.1016/j.conbuildmat.2022.130023.